UNIVERSITY OF OKLAHOMA

GRADUATE COLLEGE

BOUNDARY LAYER PROFILING USING ROTARY-WING UNMANNED AIRCRAFT SYSTEMS: FILLING THE ATMOSPHERIC DATA GAP

A THESIS

SUBMITTED TO THE GRADUATE FACULTY

in partial fulfillment of the requirements for the

Degree of

MASTER OF SCIENCE IN METEOROLOGY

By

BRIAN ROBERT GREENE
Norman, Oklahoma
2018

BOUNDARY LAYER PROFILING USING ROTARY-WING UNMANNED AIRCRAFT SYSTEMS: FILLING THE ATMOSPHERIC DATA GAP

A THESIS APPROVED FOR THE
SCHOOL OF METEOROLOGY

BY

Dr. Phillip Chilson

Dr. Christopher Fiebrich

Dr. Petra Klein

Acknowledgments

First and foremost, I would like to thank my advisor, Dr. Phil Chilson. Phil and I met in person when I was invited to visit OU for graduate school, and we instantly connected. This weather UAS project he offered me to work on was the perfect combination of my interests in physics and atmospheric sciences, and it has already taken me to new corners of the Earth. Phil's spirit and wisdom are an inspiration every day, and I am privileged to work with him. I am also grateful for the dedication and contributions from my committee members Dr. Christopher Fiebrich and Dr. Petra Klein. Their experiences in atmospheric instrumentations and observations have proven invaluable countless times, and will surely continue to do so in the future.

I am also deeply indebted to CASS engineers Tony Segales, Bill Doyle, Brent Wolf, Simon Duthoit, Arturo Umeyama, and Gus Azevedo. I am constantly amazed at the miracles you guys accomplish, and virtually all of this research hinges upon the platforms you guys have designed and built from scratch. Your countless hours soldering, welding, internet tutorial searching, and coding are truly what facilitate all of our goals, and I am proud to call you my colleagues. You guys have taught me so much about the engineering involved in this project, and it has given me a newfound respect for everything you do.

I would also like to thank James Grimsley, Dr. Robert Huck, and Dr. Elizabeth Pillar-Little for all of their CASS administrative efforts behind the scenes. This center was in its infancy when I arrived at OU, and it is already gaining international recognition thanks to the work you do to keep it running.

I have had the pleasure of collaborating with experts in instrumentation and UAS engineering, to whom I am also thankful for all of their inputs and lessons learned. The weather UAS community is growing quickly, and it is exciting to be a part of it.

Thank you as well to all of the members of the CASS research group, both past and present. Your hard work and dedication to the overall progress of CASS has not gone unnoticed.

I am grateful for Ken Carson and all of the pilots from the OU Aviation school who have served to educate us on FAA regulations and safe operations. Your course on the part 107 license material was instrumental in our operations as well. Having your expertise to navigate the world of federal policies has helped facilitate an enormous amount of research.

This project has been supported by the NSF EPSCoR grant number 1539070, the NOAA UAS Program Office, and the OU Vice President for Research Office. Thank you for investing in this exciting new field of research.

I am fortunate to have such loving friends and family who have kept me motivated throughout the graduate school experience. There have been some trying times, but you have all help keep my eyes on the prize and pick me up when I am down. My parents Jim and Diane have unconditionally supported everything I do, and I love being able to share my passion with my siblings Emily, Kevin, and Megan.

Elisa Murillo, you inspire me each and every day. You make me a better person and scientist, and I would not have made it this far without your love and support. Thank you for being my best friend.

Table of Contents

Acknowledgments **iv**

List of Tables **ix**

List of Figures **x**

Abstract **xx**

1 Introduction and Background **1**

1.1 The Planetary Boundary Layer 1

1.2 PBL Observational Systems 4

1.3 Unmanned Aircraft Systems in Atmospheric Sciences 7

1.4 CLOUD-MAP 10

1.5 UAS at the University of Oklahoma 13

2 Concept and Platforms **16**

2.1 Windsond Sensors 18

2.2 3DR Iris+ Platform 20

2.3 OU CopterSonde Platform 22

2.4 International Met Systems Sensors 23

3 System Calibration **26**

3.1 Wind Estimation 26
3.1.1 Background 26
3.1.2 Experimental Determination of Coefficients 29
3.2 Mesonet Environmental Chamber 34
3.3 Mesonet Tower 36

4 Sensor Placement **39**
4.1 Equipment 40
4.1.1 Rotary-wing Aircraft and Sensors 40
4.1.2 NSSL Mobile Mesonet 41
4.1.3 Oklahoma Mesonet hot wire anemometer 42
4.1.4 Linear actuator arm 42
4.2 Thermistor self-heating experiment 44
4.3 Anechoic chamber experiments 45
4.3.1 Setup 45
4.3.2 Procedure 48
4.4 Results and discussion 48
4.4.1 Experiment 1 - wind probe in tube 48
4.4.2 Experiment 2 - no wind probe 53

5 Field Validation **55**
5.1 EPIC Concept of Operations 56
5.2 11 May 2017 Case Study 59
5.3 Results and Summary 60

6 Boundary Layer Transitions **63**
6.1 Background 64
6.2 Data and methods 67
6.3 Results and Discussion 69

6.3.1 24 April 2018 69
6.3.2 18 October 2017 75
6.3.3 Discussion 82
6.4 Chapter Conclusions 83

7 Conclusions and Remarks **84**
7.1 Summary 85
7.2 Future Work 87

Reference List **90**

List of Tables

2.1 NOAA UAS Program Office measurement quality specifications set forth to unify standards across different instruments and UAVs. . . 19

2.2 Advertised accuracies and resolutions of the evaluated sensors. . . . 25

3.1 Summary of average iMet temperature and relative humidity sensor biases compared to NWC Mesonet tower measured in May 2017. . . 38

6.1 Summary of flights conducted at KAEFS with the OU CopterSonde 68

List of Figures

1.1 Conceptual depiction of diurnal variation in PBL structure and processes (from Scipión (2011)). 2

1.2 Adapted from Figure 1.1 to include spatiotemporal scales of different observational systems. Towers provide continuous observations but are usually confined to the surface layer. Weather balloons traverse the whole troposphere, but are usually only launched twice per day. UAS can help to fill this data gap through continuous PBL profiles. (Not to scale) 8

1.3 CLOUD-MAP team photo at the summer field campaign in Stillwater, Oklahoma, at the OSU unmanned aircraft flight station in June 2016. 11

1.4 CLOUD-MAP objective flow chart to facilitate successful research. . 11

1.5 The CopterSonde, an octo-rotor UAS designed and built by CASS at OU. This first-generation CopterSonde has been the primary mode of testing sensor placement and responses along with collecting atmospheric data since May 2017. 14

2.1 Cartoon depiction of general setup during operations, which requires a handheld transmitter and ground station communicating with the UAS. 17

2.2 Heads Up Display (HUD) screen in Mission Planner (`http://ardupilot.org/planner/docs/mission-planner-ground-control-station.html`). This screen provides information about an aircraft when connected to the ground station, including heading, battery voltage, altitude, and ground speed. This software can also be used to build flight missions and perform other diagnostics. 18

2.3 Windsond by Sparv Embedded. These thermodynamic sensors are only a few centimeters in size, making them ideal for mounting onto a UAV or releasing with a small balloon. Shown here are two packages mounted to wooden dowels, which was one of the various methods of integrating with a rwUAS. 20

2.4 The Iris+ by 3D Robotics is a quadcopter controlled by a Pixhawk autopilot and served as one of the primary experimental platforms for atmospheric research at CASS for several years. Numerous iterations of sensor placement of the Windsond probes were evaluated during this time when it was determined that response characteristics were impacted by location. 21

2.5 The iMet-XF base board (left) and bead thermistor (right) allow for modular sensor configurations. The base board provides power to the sensors and synchronizes their data streams. 23

2.6 The iMet-XF sensor package fully integrated with a Pixhawk autopilot. This setup allowed for total onboard synchronization and streaming of a single output to the ground station. 25

3.1 The standard reference frame of an aircraft, with principal axes denoted by $\hat{e}_i$. Rotation about $\hat{e}_1$ is commonly referred to as roll, $\hat{e}_2$ pitch, and $\hat{e}_3$ yaw. 27

3.2 Experimental setup for wind vector measurement calibrations. (a) Oklahoma Mesonet towers are outfitted with a propeller vane anemometer at 10 m and measure temperature at 9 m. (b) The Iris+ hovering at 10 m next to the tower, which was performed multiple times over the course of multiple days to gather a large sample of wind speeds and directions. This identical process was also performed with the CopterSonde, maintaining a constant yaw angle so as to account for differing wind attack angles relative to the UAV. 30

3.3 Relationship between 1 min averaged wind speed measured by the Washington Mesonet tower to the square root of the tangent of the vertical tilt angle on the CopterSonde. The solid red line denotes the least squares linear fit, which has a correlation coefficient of 0.7799. Data points are colored according to the flight when they were collected. 31

3.4 Wind speeds estimated in two different manners with respect to the reference 1-minute averaged Mesonet values. (a) Simple linear regression of $\sqrt{\tan(\psi)}$ yields root mean squared errors of 0.67 m s^{-1}, close to the standard requested by NOAA. (b) Linear fit with an intercept forced through the origin as an approximation of equation 3.10. This method increases RMSE relative to simple linear regression, but has a more physical relationship. 32

3.5 Estimated wind directions fit with simple linear regression (blue) compared to the ideal 1:1 line (red). A slope of 0.996 and correlation coefficient of 0.999 imply a significantly linear relationship, but a negative 12.77 intercept skews RMSE to almost 14°. This offset can likely be attributed to magnetometer interference from being in proximity to the metal Mesonet tower, which biases compass headings and therefore wind direction measurements. Otherwise, when averaged to 1-min samples, this estimation method appears robust. 33

3.6 Time series of iMet sensor A over course of calibration in environmentally controlled chamber. Temperatures ranged from -40 to +60°C over the course of about 14 hrs. 35

3.7 Calibration of 4 different iMet sensors. 36

3.8 (a) The Mesonet tower in the parking lot of the National Weather Center in Norman, Oklahoma. (b) Mounted on the tower are two aspirated chambers as reference in calibrating the iMet temperature and humidity sensors. 37

4.1 Schematic and dimensions of the rwUAS used in this study (drawing not to scale). In front and top view, the linear actuator arm is represented by the red rectangle outline, and the sensor package as a red circle. The arm was displaced from point A to point I, directly underneath the motor mounts and one pair of propellers as seen in the top-down and side views. Point B represents the tip of propeller 1, point C is directly under motor 1, D is the other side of the same propeller. Point E is halfway between the two propellers, and points F–H are symmetrical to points B–D. 43

4.2 Time series of the uncalibrated iMet temperature sensors sampling at 10 Hz relative to the times the fan was switched on (green dashed line) and off (red dashed line). 45

4.3 A: Position of linear actuator arm underneath rwUAS on mounting pedestal. Arm was aligned such that sensors passed directly underneath the motor mounts so as to make the system essentially two-dimensional. The sensor package is outlined in white. B: Close-up side view of the sensor package. The NSSL thermistor (CS 109) is strapped vertically to a foam mount so that it reaches inside the solar shield (white cylinder) from the bottom. The hot-wire anemometer is attached to the linear actuator arm with a clear mount and passes into a hole on the back side of the solar shield. C: Close-up front view of the sensor package. An iMet thermistor (PT 100) enters the solar shield through a hole on the right side. CS 109 also visible pointing vertically. 47

4.4 Experiment 1 - Time series graph of air temperature (°C) and wind speed (m s^{-1}). The background temperature is shown by the CS 109 probe (dotted black) and the iMet sensor (solid black). The CopterSonde temperatures are shown by the iMet sensor (solid blue), while the reference temperature of the CS 109 is shown in solid red. Air velocity at the CopterSonde sensor location is plotted in solid orange. Dotted green and red vertical lines indicate times when the motors were throttled on and off, respectively. Points A–I from Figure 4.1 are also indicated here. 49

4.5 Temperatures (°C) relative to NSSL background temperature at the beginning of experiment 1 to reiterate sensor self-heating. Propellers throttling on and off (green and red vertical dashed lines, respectively) seem to directly impact temperature measurements. 51
4.6 Experiment 1 time series of temperature (°C) relative to the NSSL background temperature after the actuator arm begins incrementing. Points A–I are included from Figure 4.1. 52
4.7 Experiment 2 - temperature and wind speed vs. relative time. Winds from Experiment 1 included for reference (dotted orange). Letters A–I included from Figure 4.1. 54

5.1 Concept of operations for the EPIC field campaign in May of 2017. The DOE ARM SGP site in Lamont, Oklahoma (center of yellow circle) was selected as the base of operations due to its vast array of atmospheric monitoring equipment. Oklahoma Mesonet locations (red circles) were selected based on weather forecasts for each day, and vertical profiles were performed at the SGP and selected Mesonet sites by the OU CopterSonde and Meteomatics Meteodrone rwUAS. In the meantime, the CU TTwistor fwUAS flew horizontal transects between the two locations. Flights to 2500 feet AGL were permitted within the red circles in proximity to the Mesonet sites. . 56
5.2 CU TTwistor launching from the roof of a chase vehicle (left). The Meteomatics Meteodrone hexcopter (right). These platforms, along with the OU CopterSonde, were the primary methods of sampling the PBL during EPIC. 57

5.3 Doppler radar reflectivity factor image from KVNX on 11 May 2017. The red start denotes the approximate location of the OU profiling team at each time. A: at 1830 UTC, the storm was severe-warned and was drawing inflow from the region sampled during the campaign. B: after sampling teams had ceased operations, the storm eventually produced a tornado as it passed the I-35 corridor. 59

5.4 Time-height coordinates of horizontal winds (in knots) estimated by the CopterSonde at the Marshall Mesonet site on 11 May 2018. The winds change from northwesterly background flow to northeasterly storm inflow over the course of about 90 minutes as a severe thunderstorm begins modifying its environment. 60

6.1 24 April 2018 Meteogram from the Washington Mesonet at KAEFS. The vertical red line represents the beginning of civil twilight, and the vertical black dashed lines are the first and last CopterSonde flights of the day. Top left is Temperature (°C; red) and dewpoint temperature (°C; green); top right is pressure (hPa); bottom left is wind speed (m s^{-1}) and direction (°); and bottom right solar radiation (W m^{-2}). 70

6.2 24 April 2018 potential temperature shaded and contoured in time-height coordinates. Several features are present of a classic PBL morning transition, including: stable surface layer directly after sunrise with residual layer atop; inversion height grows exponentially with time; and a well-mixed layer by 15 UTC. 71

6.3 24 April 2018 sensible heat flux (shaded) and potential temperature (contoured). Sensible heat fluxes are weakly negative in early morning. Negative fluxes follow the top of the inversion, representing the entrainment zone. Surface heat fluxes increase in time to strongly positive by 15 UTC. 72

6.4 24 April 2018 mixing ratio shaded and contoured. Exponential increase in altitude of the 7.0 g/kg isohume with time as boundary layer expands. Strong surface moisture increase starting 13 UTC and subsequent decrease an hour later as the moisture is mixed out. 73

6.5 24 April 2018 latent heat flux (shaded) and specific humidity (contoured). Strong fluxes at 13 UTC as dew and fog in the region evaporated, and subsequent decrease at 14 UTC as moisture from aloft is transported downwards. At 1430 UTC, another positive flux profile with a maximum at the top of the entrainment zone, which turns negative again by 15 UTC with further mixing. 74

6.6 18 October 2017 time series graph of data from the Washington Mesonet site. Red and black vertical lines denote same as in Figure 6.1. Similar to the case from 24 April, the morning was humid after sunrise and dewpoints stagnated after 14 UTC with mixing. There is a discontinuity in wind speed and direction at 14 UTC as momentum is rapidly transferred downwards. 75

6.7 First CopterSonde profile from 12:26 UTC on 18 October 2017 (left) in comparison to the 12 UTC sounding launched from KOUN just 30 km away (right). The black, red, and green stars at the base of the CopterSonde profile represent 2 m and 9 m temperature and 2 m dewpoint temperature measurements, respectively, from the Washington Mesonet tower closest to the profile time, which are in excellent agreement with CopterSonde temperature and dewpoint. The red box on the KOUN sounding represents the approximate same range of pressures as the CopterSonde flight, which indicates a similar strength in thermal inversion 76

6.8 18 October 2017 potential temperature as measured by the 18 rwUAS profiles shaded and contoured. Strongly stable surface layer gives way to well-mixed PBL starting around 1430 UTC. Appreciably stable zone exists at 400 m AGL atop mixed layer after the rapid transport downward of momentum due to vertical mixing. 77

6.9 18 October 2017 sensible heat flux (shaded) and potential temperature (contoured) as measured from the 18 rwUAS profiles. Alternating positive and negative heat fluxes from 1300 – 1430 UTC possibly due to alternating updrafts and downdrafts in vertical mixing. Strong negative fluxes at 14 UTC coincident with downward transport of momentum concentrated at top of the inversion layer. Positive surface fluxes at 15 UTC and subsequent well-mixed layer, with negative fluxes atop inversion implying entrainment zone. . . . 78

6.10 18 October 2017 mixing ratio measured by the rwUAS profiles contoured and shaded. Strong stratification from the surface to 200 m AGL and another zone of stratification from 500–700 m. These regions ascend and descend, respectively, until they converge around 1430 UTC with coincident pulse in surface moisture. There is a well-mixed layer afterwards with stratification above. 79

6.11 18 October 2017 latent heat flux (shaded) and specific humidity (contoured) measured from the rwUAS profiles. Weak flux magnitudes after sunrise until 14 UTC coincident with moisture pulse, and subsequent negative fluxes as moisture is mixed down with vertical mixing. 80

6.12 18 October 2017 sensible (red) and latent heat flux (blue) vertical profiles for each analysis timestep. Often times, these two mechanisms counteract one another. This is especially apparent in the 10th panel (2.16 hrs after civil twilight), which is coincident with the downward transport in sensible heat flux and momentum but surge in moisture from the surface. These both change signs again by the 12th panel (2.58 hrs), likely when vertical mixing has increased in depth. 81

Abstract

The planetary boundary layer (PBL) is comprised of energy exchanges with the Earth's surface, and as such plays a large factor in the evolution of weather conditions. However, traditional methods of observing the atmosphere, such as radiosondes and surface weather stations, considerably underrepresent processes occurring in the PBL. More recently, surface-based remote sensing capabilities have advanced, but these instruments are often expensive and difficult to implement across large scales operationally.

Using small unmanned aircraft systems (sUAS) to make atmospheric observations is rapidly being realized as a means to collect previously unobtainable observations in the lowest part of Earth's atmosphere. This study seeks to build off these advancements in technology to develop a rotary-wing sUAS (rwUAS) for collecting in-situ thermodynamic and kinematic measurements of the PBL. To do so, it is imperative to establish an understanding of the strengths and limitations of the sensors and retrieval algorithms implemented, as well as how they perform under various configurations and flight conditions. This process began with the selection of sensors capable of making high quality measurements operating standalone that were also small enough to reasonably mount onboard a rwUAS. These sensors were calibrated using an environmentally controlled chamber and validated against instrumented towers and were determined to be reliable enough moving forward to the next stage, which was integrating them with rwUASs. Having sensors perform well in a lab setting is important, but their placement onboard a rwUAS introduces additional sources of error and uncertainty. Optimal siting locations

for thermistors were examined, with results indicating that it is possible to obtain accurate measurements in the propeller wash if the sensors are adequately aspirated and motor, frictional, and compressional heating are avoided. In addition to thermodynamic measurements, a statistical model to estimate horizontal winds was derived by implementing Euler angles derived from the rwUAS's autopilot. Once these measurements were optimized individually, the systems were further validated against instrumented towers, radiosondes, and other sUASs.

Capitalizing on the intricacies of collecting meaningful observations learned through this calibration and validation, the Center for Autonomous Sensing and Sampling (CASS) at the University of Oklahoma (OU) designed and built the CopterSonde, a rwUAS optimized for thermodynamic and kinematic measurements in the PBL. This specialized aircraft allowed for the exploration of scientific objectives to determine the utility of rwUAS in the larger context of observational capabilities. The Environmental Profiling and Initiation of Convection (EPIC) was a field campaign in the spring of 2017 that demonstrated the capability of UASs to provide forecasters with quasi-real time profiles of pre-convective environments. Furthermore, a method of evaluating vertical heat flux profiles during diurnal PBL transitions was examined. The results presented herein represent foundational efforts towards developing the infrastructure required for successful rwUAS operations. To conclude, an outlook for tapping into the serviceability of rwUAS for atmospheric sciences is discussed.

Chapter 1

Introduction and Background

1.1 The Planetary Boundary Layer

The planetary boundary layer (PBL) is the lowest layer of the troposphere which exchanges energy with the Earth's surface on timescales of less than one hour (Stull, 1988), and acquiring atmospheric measurements in this region has proven to be challenging (National Research Council, 2009; Hardesty and Hoff, 2012). Forcings such as radiative transfers, frictional dissipation, and evaporative cooling combine to modify the PBL with diurnal periodicity (Figure 1.1). For instance, as the sun rises and begins warming the surface via shortwave radiation, turbulence develops and mixes heat and momentum throughout the expanding PBL. As the solar elevation angle decreases towards sunset, turbulence decays as the ground cools faster than the air directly above, inducing stable stratification. With the vertical transport in momentum diminished, this stable layer can decouple from the residual layer aloft, becoming effectively stationary with only intermittent turbulence (Stull, 1988).

Due to spatiotemporal heterogeneities in energy exchanges, the PBL can be further categorized into various sublayers. The lowest 10% or so of the PBL is known as the surface layer, where vertical fluxes are approximately constant with height and wind speed, temperature, and moisture assume logarithmic profiles

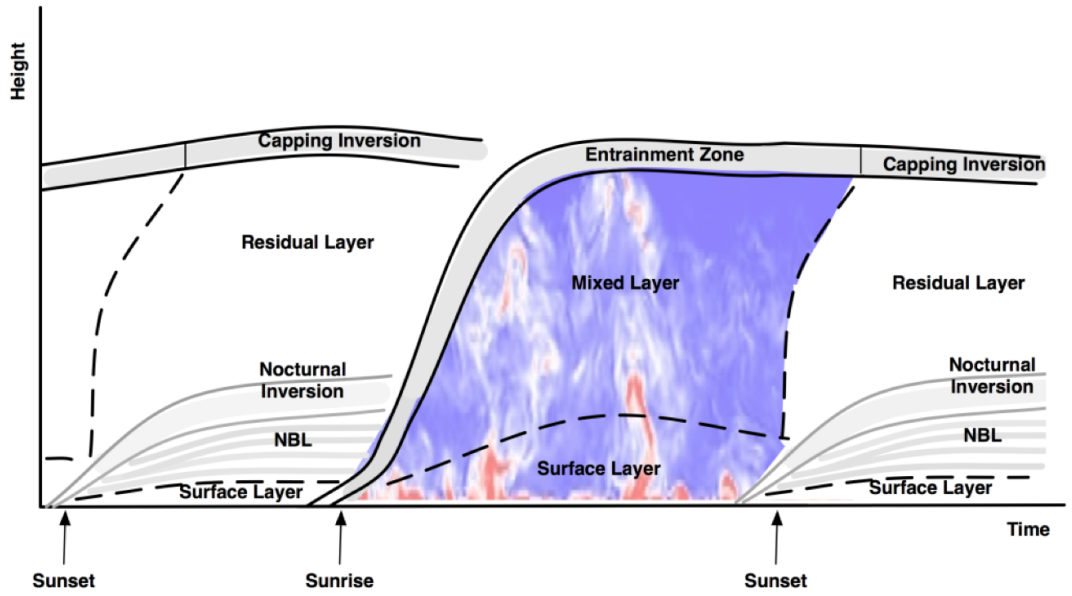

Figure 1.1: Conceptual depiction of diurnal variation in PBL structure and processes (from Scipión (2011)).

(Garratt, 1992). During the day, the remainder of the PBL above the surface layer is convectively mixed and vertically homogeneous in momentum, potential temperature, and mixing ratio. In the evenings, the stratification in the PBL is not always as transparent. With calm winds, temperature changes are dominated by longwave cooling near the surface which causes temperature to increase with height. Exceptions to this model include cloudy nights, which also radiate heat downwards, counteracting the effective surface cooling. Furthermore, spatial heterogeneities in land surface type can influence cooling and moistening rates overnight, which in turn can promote the development of localized flows. Complex terrain can induce drainage flows into valleys and create disturbances in flows across hilltops, further compounding the vertical structure of the nocturnal PBL (Wood, 2000; Shapiro and Fedorovich, 2007). In the Great Plains region of the United States, baroclinicity across sloping topography can induce a low-level jet (LLJ) overnight (Bonner, 1968) that is characterized by wind speeds greater than geostrophic flow.

This feature is commonly located below one kilometer above ground level (AGL), and is often associated with nocturnal convection events (Reif and Bluestein, 2017).

Understanding PBL processes is vital to a proper understanding of larger-scale weather phenomena, since turbulent eddies ranging in size from kilometers to millimeters redistribute momentum, heat, and moisture. These local heterogeneities can impact regions of cloud cover and storm development, frontal propagation, and low pressure system intensification, all of which are pertinent to forecasters. For example, Nowotarski et al. (2011) demonstrated that thermodynamic stratification in the boundary layer in proximity to supercell thunderstorms can significantly impact updraft strengths and low level vorticity fields, and Sinclair et al. (2012) provides insight to the complexity of low-level frontal structure. Markowski (2016) explores the significance of surface drag on development of vertical vorticity in supercell thunderstorms. Markowski and Bryan (2016) discuss the importance of large eddy simulation (LES) PBL schemes to be able to accurately depict turbulence with regards to simulation accuracy.

Recently, wind energy has been a rapidly-developing sector of the world economy, making it imperative to understand and predict boundary layer winds. Climatologies of prevailing winds is important in designing the dimensions of wind turbines, and complexities in terrain can create a challenge when determining individual siting (Zhou and Chow, 2012). Optimization of energy production based on interactions of downstream wake propagation in wind farms is of great interest to energy companies, who need to be able to adjust power output from other sources accordingly. As the world turns to renewable energy as a means to reduce greenhouse gas emissions, companies must be able to maximize their energy production. This endeavor will require sufficient wind forecasts, which can be improved through better observations of the PBL.

Formation and persistence of fog can significantly impact the transportation of goods and services, which results in large economic losses for these companies. Furthermore, conditions with reduced visibility cause around 700 driving fatalities per year in the United States (Ashley et al., 2015). Numerical weather prediction (NWP) models have relatively low skill in forecasting fog, which is largely dependent on boundary layer parameterization schemes (Steeneveld et al., 2015, and references therein). A better understanding of the boundary layer and its role in fog development would improve predictive capabilities, thereby mitigating the associated economic impacts.

Boundary layer processes are also of great interest to public health, as it is the region of the atmosphere in which humans live. Pollutants disperse in the atmosphere as passive scalars, and can get trapped in a temperature inversion during PBL transitions. According to the World Health Organization (2016), air pollution was estimated to cause 3 million premature deaths worldwide in 2012. With a better understanding of particle dispersion in boundary layer flows, air quality forecasts can be made more accurately and further in advance so people can prepare accordingly.

1.2 PBL Observational Systems

Boundary layer flows are highly complex and nonlinear in space and time, even with several layers of assumptions applied in theory. As such, it has always been a challenge for meteorologists to collect representative measurements of the environment, even with continual advances in technology. One of the most common resources for PBL studies has been instrumented towers, which can continually provide data at a point location over long periods of time. For example, Charba (1974) examined thunderstorm outflow characteristics in comparison to laboratory

density current observations by using a 444 meter tall tower instrumented at several heights to collect vertical cross-sections. Shapiro (1984) analyzed a cold front using the 300 meter tower in Boulder, Colorado, and discussed how its structure was capable of triggering new convection. Poulos et al. (2002) used a highly instrumented 60 meter tower to calculate fluxes and other PBL processes in the stable nocturnal boundary layer. The Oklahoma Mesonet (Brock et al., 1995; McPherson et al., 2007) is a network of 120 instrumented 10 meter towers across the state of Oklahoma, and collects surface observations every five minutes year-round. These observations form a climatology of Oklahoma weather dating back to the 1990s, and have been the focus of hundreds of scientific studies (Van der Veer Martens et al., 2017). While highly reliable and configurable, instrumented towers do come with an inherent downside. Being limited in vertical extent, the convective boundary layer often extends well above even the tallest of towers. Networks with the horizontal resolution of the Mesonet still cannot provide details on the vertical structure of the atmosphere.

Presently, weather balloons are the most common tool available for in-situ observations above the level of towers. They provide valuable kinematic and thermodynamic data from the upper atmosphere, which impacts both short-term weather forecasts (Cohen et al., 2007; Faccani et al., 2009; Lackmann, 2011) as well as climatological trends (Luers and Eskridge, 1998; Lanzante et al., 2003; Thompson and Solomon, 2005) and can serve as a baseline for model verification (Agustí-Panareda et al., 2010; Benjamin et al., 2010; Gensini et al., 2014). Rawinsondes are launched in hundreds of locations around the world every day, although usually only twice a day at most sites. This operational network is also not suited to provide adequate PBL measurements, as they ascend too rapidly through the lowest levels (National Research Council, 2009). More frequent deployments with slower ascents are commonly performed on field campaigns (e.g., Kosiba et al.,

2013; Parker, 2014; Trapp et al., 2016; Geerts et al., 2017), but this becomes expensive as the sensor package is rarely recovered for reuse. Specialized satellite remote sensors can derive vertical thermodynamic and kinematic profiles across significant areas of the Earth, but vertical resolutions in the PBL are too coarse for practical application.

Surface-based remote sensors such as wind profilers, Doppler lidars, sodars, and radiometers are capable of continuously observing a fixed location (e.g., Grund et al., 2001; Poulos et al., 2002; Banta et al., 2015; Bonin et al., 2015; Lundquist et al., 2017; Toms et al., 2017; Geerts et al., 2017; Blumberg et al., 2017), but rely on numerous assumptions about the atmosphere and have trouble resolving measurements close to the surface. These types of instruments are also cost-prohibitive when considering expansion to larger-scale networks such as the global upper-air sites.

Even when combining surface towers, balloons, and remote sensors with other observational techniques such as tethered balloons, Doppler weather radars, and satellite remote sensors, the National Research Council (2009) still concluded that the "vertical component of U.S. mesoscale observations is inadequate." The NRC in this report implored government agencies to pursue developments in capabilities to monitor the lower atmosphere at finer scales in space and time. Fortunately, unmanned aerial vehicles (UAVs, a subset of the more general term, unmanned aircraft systems (UASs)) appear to resolve some of these issues, which is detailed in Section 1.3.

1.3 Unmanned Aircraft Systems in Atmospheric Sciences

Capitalizing on the recent commercial accessibility of UAVs and miniaturized sensor packages, numerous groups around the world have embraced the potential for integrated platforms to fill this atmospheric data void (e.g., Reuder et al., 2009; Houston et al., 2012; Lothon et al., 2014; Wildmann et al., 2014; Vömel et al., 2018). UAVs have the notable advantage of being able to operate in regions beyond the reach of typical systems, including environments that may be dangerous. Sophisticated systems can be deployed on a regular basis for consistent measurements, and they are less expensive alternatives to ground-based remote sensors measuring similar parameters. They can be used for a variety of missions measuring different quantities, such as horizontal transects across airmass boundaries or continuous vertical profiling at fixed ascent rates (Figure 1.2). Because of these advantages, the National Research Council (2007) stated that UAV "technology should be increasingly factored into the nation's strategic plan for Earth science."

The concept of utilizing remote controlled aircraft (RCA) to take atmospheric measurements has been around for nearly half a century (Konrad et al., 1970). Back then, mounting sensors onto an RCA posed a significant challenge, as the instruments were large and heavy. In recent years, technological advancements in manufacturing and signal processing have led to miniaturization of sensors down to the size of centimeters and weighing only a few grams. In conjunction with the recent commercialization of UAS and open source autopilot software, atmospheric scientists in the past few decades have begun to realize the potential for using UAS to sample the lower atmosphere.

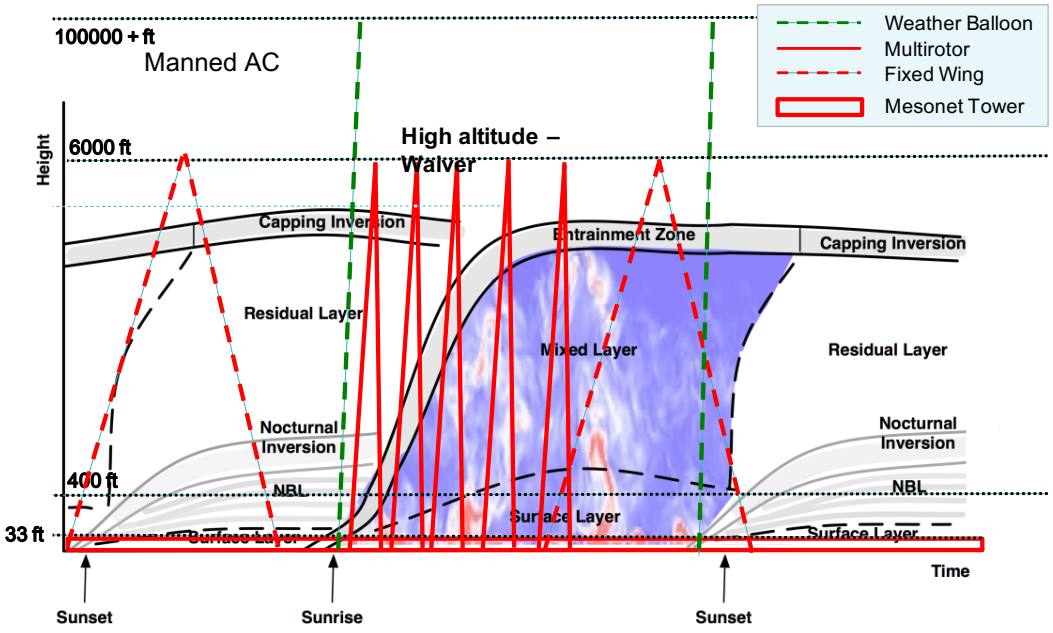

Figure 1.2: Adapted from Figure 1.1 to include spatiotemporal scales of different observational systems. Towers provide continuous observations but are usually confined to the surface layer. Weather balloons traverse the whole troposphere, but are usually only launched twice per day. UAS can help to fill this data gap through continuous PBL profiles. (Not to scale)

Several groups have experimented with fixed-wing UAS (fwUAS) for research in the PBL. For example, Reuder et al. (2009, 2012) developed the Small Unmanned Meteorological Observer (SUMO) based on a foam pusher propeller plane to sample temperature, pressure, and humidity. The SUMO has had numerous recent successes in field campaigns, including the Boundary-Layer Late Afternoon and Sunset Turbulence (BLLAST) field campaign in France in 2011 (Lothon et al., 2014; Båserud et al., 2016). The SUMO was also the inspiration for the Small Multifunction Autonomous Research and Teaching Sonde (SMARTSonde) project at the University of Oklahoma (OU) (Chilson et al., 2009). This platform has been used in numerous applications including the estimation of heat flux profiles (Bonin

et al., 2012), structure function estimations (Wainwright et al., 2015), wind vector estimations (Bonin et al., 2013), and ozone concentrations in the PBL (Zielke, 2011). At the Eberhard-Karls-University Tübingen in Germany, Wildmann et al. (2014) developed the Multipurpose Airborne Sensor Carrier (MASC) for PBL measurements at high enough resolutions to directly resolve turbulent processes for use in wind energy research. Houston et al. (2012) have demonstrated the infrastructure required to combine meteorology, engineering, and policy to conduct PBL research with UAVs specifically in the United States airspace. Several other groups successfully experimented with UAS technology (e.g., de Boer et al., 2016; Bailey et al., 2017; Vömel et al., 2018), and funding agencies such as the National Science Foundation (NSF) in the United States have encouraged collaboration between universities (Chilson et al., 2016; Jacob et al., 2018).

Owing in part to the longstanding history of manned research aircraft, fixed-wing UASs (fwUASs) have been at the forefront of UAS development for atmospheric research (Saïd et al., 2005; Gioli et al., 2006; van den Kroonenberg et al., 2012). However, fwUASs come with several notable disadvantages, namely their inability to sample a vertical column at a fixed horizontal position, risks when operating close to the ground, and the need for a suitable surface for landing and possibly takeoff. Currently, rotary-wing UASs (rwUASs) are being proven to be a viable supplement to fwUASs thanks to their autonomous vertical takeoff/landing capabilities (Brosy et al., 2017; Vömel et al., 2018). Integration of rwUAS with observational networks and research efforts has the potential to vastly improve our understanding of processes occurring in the lowest regions of the atmosphere at unprecedented scales.

1.4 CLOUD-MAP

The Collaboration Leading Operational UAS Development for Meteorology and Atmospheric Physics (CLOUD-MAP) project, supported by the National Science Foundation's (NSF) Established Program to Stimulate Competitive Research (EPSCoR), is a four year, six million dollar project awarded in 2015 to collaborators from Oklahoma State University (OSU), the University of Oklahoma, the University of Nebraska-Lincoln (UNL), and the University of Kentucky (UK; Figure 1.3). This project is designed as a testbed for pioneering effective integration of UAVs with atmospheric sciences, and is one of the first of its kind on this magnitude (Chilson et al., 2016; Jacob et al., 2018). This significant investment by the NSF aligns with recent reports from the National Research Council (2007, 2009) calling for increased UAS technology in Earth sciences to address the inadequacies of current observational networks. As mentioned before, the prospect of using UAS for atmospheric research has been researched for decades, but CLOUD-MAP offers the opportunity for a multi-disciplinary approach to examine a broad swath of topics. With expertise from the participating universities in robotics, UAS, meteorological instrumentation, and atmospheric modeling, CLOUD-MAP seeks to determine how atmospheric data acquired by UAS could be used to better understand weather phenomena, how UAS might be able to detect large-scale weather trends, and the required operational designs necessary to implement UAS on a regular basis.

To answer these basic questions, four specific objectives are proposed with research tasks to be supervised by the principal investigators (PIs) at each university. These objectives are designed to flow from one to another in a manner that encourages collaboration between universities (Figure 1.4). The primary objective is to develop a mentorship for early-career faculty with relevant expertise in atmospheric observations with UAS. Establishing an environment that encourages

Figure 1.3: CLOUD-MAP team photo at the summer field campaign in Stillwater, Oklahoma, at the OSU unmanned aircraft flight station in June 2016.

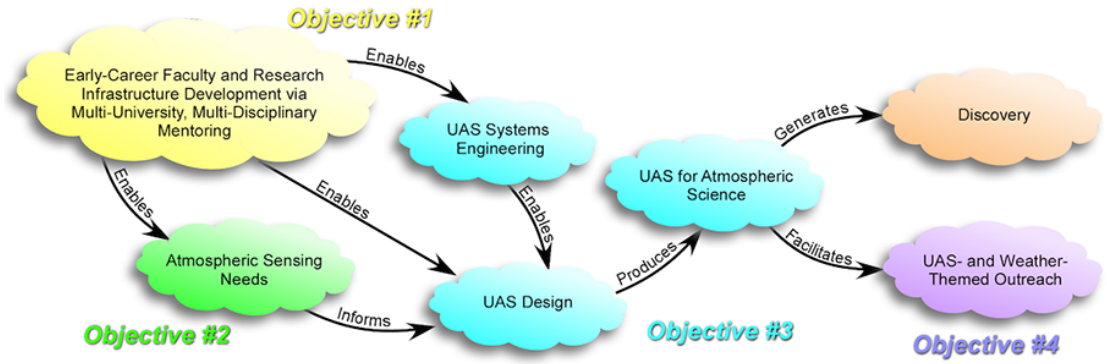

Figure 1.4: CLOUD-MAP objective flow chart to facilitate successful research.

participation from students enables the faculty to be more successful in advancing the science. The second objective focuses on the development and application of UAVs for use in atmospheric sensing, which includes testing with different sensors, platforms, mission designs, and communication technologies. This core component of the CLOUD-MAP mission inspired and funded the work in this study, and facilitated several investigations by the other collaborators. The third objective involves the optimization of communication and control capabilities of UAS, which explored the engineering required to support the atmospheric science-driven objectives. For safe and routine operations in the national airspace, it is essential to have robust communications between the ground station and aircraft at all times.

Furthermore, to support sampling in a heterogeneous environment, one approach involves a network of spatially distributed platforms communicating with one another. Finally, the fourth CLOUD-MAP objective is to improve national education on UAS technology through outreach. One facet of this objective involves K-12 activities that promote science, technology, engineering, and mathematics interest such as education on basic weather phenomena, UAS utility for measuring the environment, and the basics of electrical, aerospace, mechanical, and computer engineering required to facilitate operations.

The CLOUD-MAP project is a revolutionary investment from the NSF both financially and scientifically. Support of this magnitude transparently portrays how much the United States believes in the technology, as it lays significant groundwork for future endeavors. Addressing the objectives outlined previously has allowed CLOUD-MAP to greatly contribute to the community of scientists and engineers experimenting with UASs in atmospheric sciences. Integrating UASs into the national airspace for research has proven to be a complex problem spanning many disciplines, which is largely why the objective-oriented approach of this project has been successful. Not only does this collaboration include the four main universities of OSU, OU, UNL, and UK, it also has significant contributions from other experts in the fields of atmospheric physics and UAS engineering. These partnering institutions include the National Aeronautics and Space Administration (NASA), the National Center for Atmospheric Research (NCAR), the National Oceanic and Atmospheric Administration (NOAA), the University of Colorado, Massachusetts Institute of Technology, and private companies Aerospace Corporation, Blackswift, Piasecki, and FLIR. Drawing expertise from these partners has allowed CLOUD-MAP to maximize its impact on the community, which will have rippling effects for years to come.

1.5 UAS at the University of Oklahoma

It is apparent that UAS technology has great potential to fill the data gap in lower atmospheric observations. To realize this potential, this study seeks to design and implement a rotary-wing UAS capable of vertical thermodynamic and kinematic profiling. To do so, development has been segmented into three primary components. First, thermodynamic sensors small enough to fit on a UAV and also offering high quality measurements were selected and calibrated to determine their reliability. Second, these sensors were integrated with the platforms, and their new responses and uncertainties were quantified. Such optimization included the issue of sensor placement along with calibration of wind vector estimations. Finally, once the platforms were capable of operations, measurements were taken in the field and validated against other instruments and theory to ensure results were physical and not artifacts of the system.

This development has required proficiency across the disciplines of engineering and meteorology, and has been a catalyst for the creation of the Center for Autonomous Sensing and Sampling (CASS) at OU. Established in 2016 under the auspices of the Vice President for Research Office, CASS's mission is to explore, advance, and develop complete adaptive and autonomous sensing and sampling systems for use in the atmosphere, on the ground, and in the water, and to help facilitate the integration of this technology across various disciplines and institutions.

To meet the growing demand for PBL observations, CASS has experimented with and designed several unmanned aerial vehicles (UAVs) and sensor packages, which will be outlined in more detail in Chapters 2 and 3. To ultimately move towards unattended autonomous profiling, CASS developed and manufactured the CopterSonde (Figure 1.5), which is an rwUAS outfitted with a Pixhawk autopilot

Figure 1.5: The CopterSonde, an octo-rotor UAS designed and built by CASS at OU. This first-generation CopterSonde has been the primary mode of testing sensor placement and responses along with collecting atmospheric data since May 2017.

(3D Robotics), four temperature, and four relative humidity sensors for thermodynamic profiling (Section 2.3). Sensor integration with the CopterSonde posed a key challenge to ensure proper representation of the sampled environment, and much care has been taken to optimize their locations (Chapter 4; Greene et al., 2018). Furthermore, by utilizing rotational angles from the Pixhawk's intertial measurement unit (IMU), the CopterSonde is capable of measuring the horizontal wind vector during vertical profiles (Section 3.1).

The CopterSonde's ability to sample thermodynamic and kinematic profiles of the PBL has been put to the test on numerous occasions (Chapters 5 and 6). Beginning with the Environmental Profiling and Initiation of Convection (EPIC) field campaign in May 2017, continuous profiling in pre-convective environments in North-Central Oklahoma was performed with data being sent back to the National Weather Service in Norman in real time. This experiment was an example to the National Oceanic and Atmospheric Administration (NOAA) of how UAS could be utilized in day-to-day operations. Later that summer, in June 2017, the CopterSonde flew in conjunction with several platforms from collaborators on the NSF

CLOUD-MAP project, as a collaborative effort to compare how measurements respond between the platforms and against other ground-based instruments. Finally, the CopterSonde has flown profiles to investigate morning PBL transitions at the Kessler Atmospheric and Ecological Field Station in Purcell, Oklahoma. Results from each of these individual campaigns have provided insight both from a meteorological perspective but also in terms of streamlining operations and implementing more effective platforms. The capabilities of CASS extend well beyond the first generation CopterSonde discussed herein (and beyond just atmospheric sensing as well), but these largely stem from the knowledge and experiences gained from its development and utilization.

Chapter 2

Concept and Platforms

Flying UASs and collecting atmospheric observations is a multi-faceted, interdisciplinary task. Ultimately, the end product yields datasets to be interpreted by atmospheric scientists; however, this is only one small piece of the puzzle. Designing platforms to fly and synthesize meteorological sensors with flight controllers requires expertise in aerospace, mechanical, and electrical engineering. Autopilot customization with a ground station streaming and saving data in real time is accomplished through proficiency in computer science. Operating UAVs in the National Airspace System (NAS) also requires significant coordination with the Federal Aviation Administration (FAA) and university risk management, which is streamlined through collaboration with privately licensed pilots. Key details such as sensor placement, mission design, and deployment strategies also necessitate an understanding of atmospheric physics. Fortunately, CASS has grown to encompass this array of disciplines in its employees, and continues to improve its scientific capabilities.

The nature of this project strongly encouraged experimentation with different commercially available platforms and sensor packages. This ultimately led to dozens of different variations on sensor integration, a few of which will be discussed in this chapter. Vertical profiling missions typically consisted of a rwUAS (with

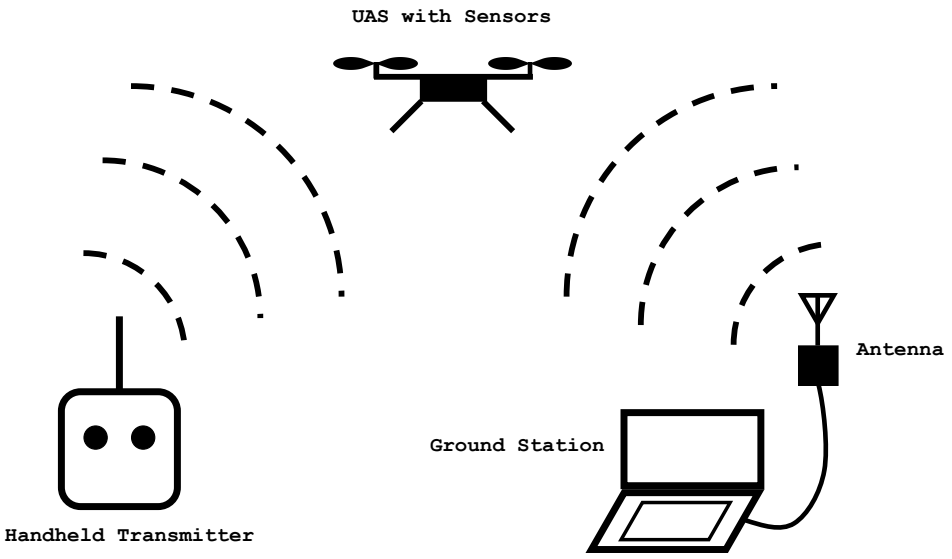

Figure 2.1: Cartoon depiction of general setup during operations, which requires a handheld transmitter and ground station communicating with the UAS.

integrated thermodynamic sensors) controlled by the aircraft's autopilot and communicating through radio frequency to a computer ground station (Figure 2.1). A human operator was also present with a hand held radio transmitter to arm the motors prior to takeoff, but otherwise only was necessary as a safety backup since flight missions were pre-configured using the open-source Mission Planner software (Figure 2.2) and written to the Pixhawk autopilot to be flown automatically.

Missions were built by defining waypoints in latitude, longitude, and altitude, and status of the UAV could be monitored in real time with Mission Planner. Each specific combination of platform and sensors necessitated a unique ground station setup, and it was found that systems were more reliable with fewer data streams involved.

Selection of a platform and sensors is the first major step in development of a UAS for atmospheric sampling. This begins with sensors that offer high quality measurements and are robust enough to be mounted on a UAS. Furthermore,

Figure 2.2: Heads Up Display (HUD) screen in Mission Planner (`http://ardupilot.org/planner/docs/mission-planner-ground-control-station.html`). This screen provides information about an aircraft when connected to the ground station, including heading, battery voltage, altitude, and ground speed. This software can also be used to build flight missions and perform other diagnostics.

it requires a platform sturdy enough to withstand atmospheric conditions and customizable enough to meet data acquisition requirements. The NOAA UAS Program Office has set forth guidelines for data quality standards (Table 2.1), which has served as the benchmark for this study.

2.1 Windsond Sensors

One of the first sensor packages CASS tested was the Windsond by Sparv Embedded (Figure 2.3). An individual sensor consisted of a base circuit board with

Table 2.1: NOAA UAS Program Office measurement quality specifications set forth to unify standards across different instruments and UAVs.

Meteorological Variables and Accuracies	
Temperature	$\pm$ 0.2°C
Relative Humidity	$\pm$ 5.0%
Pressure	$\pm$ 1.0 hPa
Wind Speed	$\pm$ 0.5 m s^{-1}
Wind Direction	$\pm$ 5° Azimuth
Sensor Response Time	
Time	$<$ 5 s (preferably $<$ 1 s)
Operational Environmental Conditions	
Temperature	$-30 - 40°$ C
Relative Humidity	$0 - 100\%$
Wind Speed	$0 - 45$ m s^{-1}

a removable extension that altogether measured GPS location, pressure, temperature, and relative humidity at 1 Hz and streamed live to a ground station with provided software, and optionally logged data onboard. While their miniature size and advertised specifications met the NOAA guidelines (Table 2.2), several months of testing exposed some key weaknesses. The electrical components of the circuit board, namely the GPS and telemetry antennae, were often unreliable. The devices required a full GPS signal before they would record data, which could sometimes take over 10 min to acquire. Furthermore, they would commonly lose signal to the ground station. Because data were not logged on the sensors themselves and only saved on the ground station for our operations, this created gaps in data that

Figure 2.3: Windsond by Sparv Embedded. These thermodynamic sensors are only a few centimeters in size, making them ideal for mounting onto a UAV or releasing with a small balloon. Shown here are two packages mounted to wooden dowels, which was one of the various methods of integrating with a rwUAS.

could occasionally last the majority of a mission. These sensors were also relatively fragile, and extended use brought the degradation of circuit connections and battery life, rendering them unresponsive. Finally, each sensor required its own connection to the base station, so mounting several sensors on a platform for comparisons would often cause interference in communications. Although the version tested was not reliable enough for integration operationally, the Windsond sensors still provided a necessary avenue for scientific development with several valuable lessons learned. These sensors have since been upgraded by Sparv Embedded, but we have not performed extensive testing with the newer models.

2.2 3DR Iris+ Platform

At the time of this writing, there are hundreds (if not thousands) of rwUAS available for purchase, each of varying quality and included accessories. Many of these are controlled with proprietary software and autopilots that do not lend themselves

Figure 2.4: The Iris+ by 3D Robotics is a quadcopter controlled by a Pixhawk autopilot and served as one of the primary experimental platforms for atmospheric research at CASS for several years. Numerous iterations of sensor placement of the Windsond probes were evaluated during this time when it was determined that response characteristics were impacted by location.

to the level of customization necessary for research missions. Fortunately, there are a number of platforms that make use of the open source Pixhawk autopilot. The Iris+ by 3D Robotics (Figure 2.4; no longer in production) is one such platforms, and was one of the first rwUAS tested by CASS. With a brand new battery, it can achieve flight times around 15–20 min, which is more than enough time to traverse the 120 m vertical limit imposed by the FAA part 107 license regulations. The Iris+ equipped with a suite of Windsond sensors served as a testbed for experimenting with how to fly UAVs manually, different flight patterns and sensor placements, and estimating winds with the method described in Section 3.1. After several months of flights and iterations of sensor integration (each with their own varying results) we realized that obtaining representative thermodynamic measurements was not as straightforward as placing the sensors wherever they fit best on the UAV. This eventually led to an objective analysis of measurement error sources induced by a rwUAS itself, which is covered in Chapter 4.

Eventually, we determined that the Iris+ would require an upgrade for obtaining regular PBL measurements. Being a small quadcopter made of plastic with weak motors and shallow propellers meant it was unable to withstand wind speeds regularly observed in Oklahoma. Its battery life was not long enough to endure profiles through the entire convective boundary layer (CBL), which yields an incomplete atmospheric perspective. When combined with four Windsond sensors, the ground station had to maintain five separate lines of communication to the platform during flights, which rarely remained continuous. Post processing all of the irregular data streams therefore produced noisy results inconsistent with the NOAA specifications. Other commercially available rwUASs also lacked the customizability in mission planning and sensor integration desired for operations when compared with the Iris+. This led to the conclusion that a UAS fabricated in-house was necessary.

2.3 OU CopterSonde Platform

Building upon the strengths of the Iris+ system, CASS engineers designed and built the CopterSonde rwUAS (Figure 1.5). The CopterSonde facilitates a symmetrical carbon fiber hashtag design with a diameter of 65 cm and is driven by eight brushless electric motors and 25 cm diameter propellers. The maximum payload mass amounts to 1 kg with a total all-up weight of about 7 kg. The maximum flight time is about 20 minutes. It has a top flight speed of 25 m s^{-1} and thus can be flown safely in winds up to a maximum horizontal speed of 20 m s^{-1}. The CopterSonde is equipped with a Pixhawk autopilot (3D Robotics, Inc.) which relies on an on-board inertial measurement unit (IMU) for attitude estimation. A barometric pressure sensor is used to control the altitude of the rwUAS. The CopterSonde also carries a post-processing kinematic differential GPS unit which gives centimeter positioning accuracy in space. External sensor data are sent to

the Pixhawk via the I^2C protocol, which are processed in parallel to the flight controls. This setup allows for a single consolidated data stream sent to the ground station over wireless radio using the Mavlink protocol. The operative distance of the communication system is around 5 km, capable of 15 km with upgraded antennae. The CopterSonde has been extensively calibrated and tuned for field measurements, with much consideration taken for sensor placement (Chapter 4) and optimization of data streaming.

2.4 International Met Systems Sensors

As an alternative to the Windsond sensors, the CopterSonde platform made use of PT 100 bead thermistors from International Met Systems (iMet; Figure 2.5) and capacitive humidity sensors produced by IST. These bead thermistors offer a response time of 2 s in still air (approximately 1 s with 5 m s^{-1} aspiration) over a range of -95 to +50°C, with an accuracy of ± 0.3°C and a resolution of 0.01°C (see Table 2.2 for comparisons to the Windsond specifications). The humidity sensors advertise a response time of under 10 seconds and also measure temperature with a similar response. These sensors are similar to the kind used on many standard radiosondes and are ideal for use on a rwUAS.

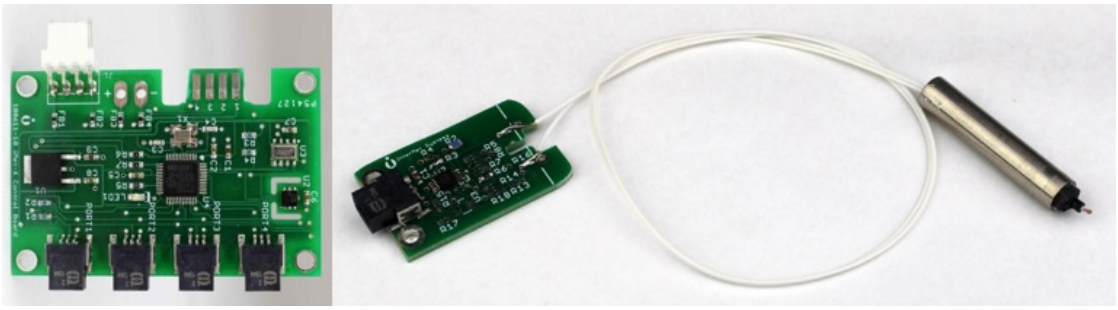

Figure 2.5: The iMet-XF base board (left) and bead thermistor (right) allow for modular sensor configurations. The base board provides power to the sensors and synchronizes their data streams.

The sensors are components of a bigger iMet system specifically designed for UAV applications: the iMet-XF UAV. This system uses a main board to which different types of thermodynamical sensors can be interfaced. It samples each connected sensor successively, including on-board GPS and pressure sensors, and provides these data in packets through serial communication. Acquiring and storing the data can be achieved in a variety of ways: using a pair of radios to stream data to a ground station, or the unit can be connected to a computer for direct data streaming using the provided iMet software.

The consolidation of sensor data into one stream significantly improves the iMet-XF reliability over the Windsond sensors. However, due to the proprietary signal processing on the control board, transmission of this data required an on-board microprocessor and ground station radio link in addition to the autopilot and telemetry link. To further reduce the number of electronic components requiring power and potentially causing interference, the provided base board was bypassed with a custom circuit board. Taking advantage of the fact that the iMet sensors include their own integrated circuit boards that convert analog data streams into the common I^2C protocol, this custom board was capable of accepting and synchronizing eight separate sensor inputs and converting them into a single output stream. On the CopterSonde, this amounted to four temperature and four humidity sensors being synchronized at once. By inputting this single data stream into the Pixhawk flight controller, a specially configured module was programmed to sample each sensor successively at a given rate, log their data on-board, and stream live data to the ground station (Figure 2.6).

With virtually no impact on flight performance, this implementation of sensors through the autopilot streamlined operations immensely. Onboard synchronization and a single data stream yielded only a single data file after each flight, which was easily readable for post processing. Combined with the overall reliability of

the sensors (Chapter 3), this setup evolved to be the operational version of the CopterSonde for research.

Figure 2.6: The iMet-XF sensor package fully integrated with a Pixhawk autopilot. This setup allowed for total onboard synchronization and streaming of a single output to the ground station.

Table 2.2: Advertised accuracies and resolutions of the evaluated sensors.

	Windsond		iMet-XF	
Variable	Accuracy	Resolution	Accuracy	Resolution
Temperature (° C)	± 0.3	0.01	± 0.3	0.01
Relative Humidity (%)	± 2.0	0.05	± 1.8	0.03
Pressure (hPa)	± 1.0	0.02	N/A	N/A
Max Sample Rate (Hz)	1		10	

Chapter 3

System Calibration

While many of the observational techniques outlined in Section 1.2 may not adequately meet the growing demands of lower atmospheric observations, they are still held in high regard for their quality standards. Ideally, measurements from UAVs should be able to emulate those from observational networks that can run continuously around the clock for years on end both in terms of consistency and representativeness. These UAVs should also be able to do so with relatively low maintenance. Once a platform and sensor suite has been selected, one must dedicate time to calibrating them to attain research quality observations. For thermodynamic and kinematic measurements using the multicopters and sensors outlined in Chapter 2, this process involved calibrations in environmentally controlled chambers and comparisons against instrumented Oklahoma Mesonet towers.

3.1 Wind Estimation

3.1.1 Background

As one application, rotary-wing UAS can be used to measure the same thermodynamic and kinematic properties as radiosondes: pressure, temperature, relative humidity, and horizontal wind speed and direction (Neumann and Bartholmai,

2015; Brosy et al., 2017). The thermodynamic measurements are collected directly, with sensors mounted on the platform itself. However, in the approach adopted by the CopterSonde, the wind vector is not measured directly as in the case of fixed-wing aircraft with a multi-hole probe (e.g., Bonin et al., 2013). Instead, winds are estimated using the geometry of how the UAV tilts into the wind to maintain a fixed latitude-longitude position while in flight. This method, similar to that outlined by Neumann and Bartholmai (2015) and Palomaki et al. (2017), proceeds as follows.

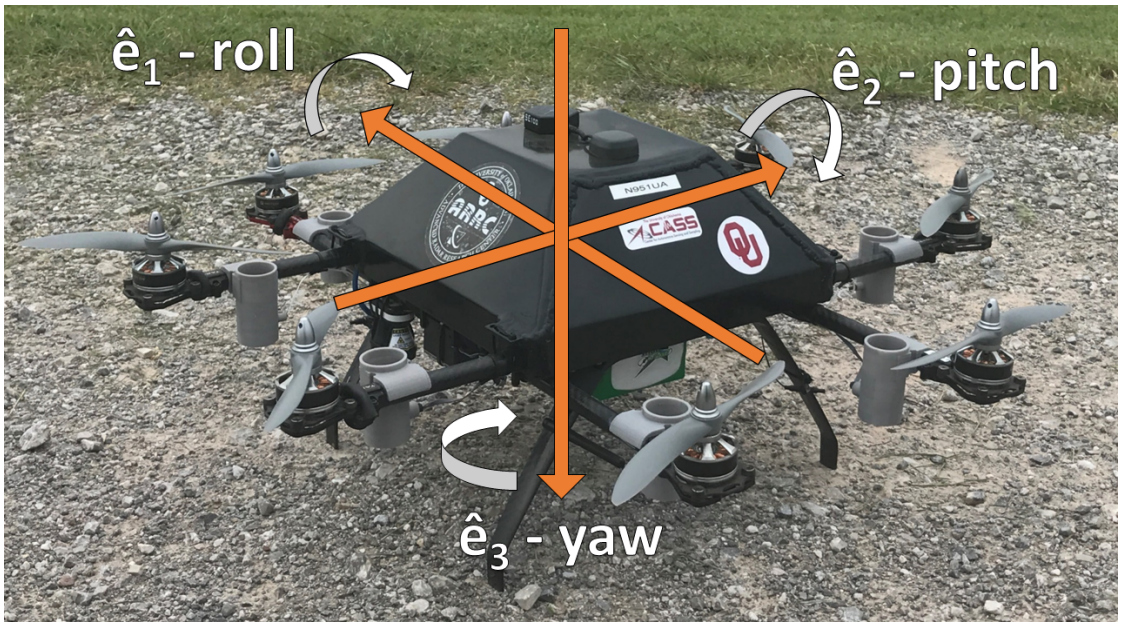

Figure 3.1: The standard reference frame of an aircraft, with principal axes denoted by $\hat{e}_i$. Rotation about $\hat{e}_1$ is commonly referred to as roll, $\hat{e}_2$ pitch, and $\hat{e}_3$ yaw.

The inertial measurement unit onboard the Pixhawk autopilot system records the UAV's roll, pitch, and yaw rotation angles (also known as attitude) (Figure 3.1). By taking the lab reference frame as the base coordinates, one can interpret the attitude as a rotated coordinate system. Taking into account the geometry of the UAV's reference frame, the x, y, and z rotation matrices are therefore expressed as:

$$R_x = \begin{bmatrix} 1 & 0 & 0 \\ 0 & \cos(roll) & \sin(roll) \\ 0 & -\sin(roll) & \cos(roll) \end{bmatrix}, \tag{3.1}$$

$$R_y = \begin{bmatrix} \cos(pitch) & 0 & -\sin(pitch) \\ 0 & 1 & 0 \\ \sin(pitch) & 0 & \cos(pitch) \end{bmatrix}, \tag{3.2}$$

$$R_z = \begin{bmatrix} \cos(yaw) & -\sin(yaw) & 0 \\ \sin(yaw) & \cos(yaw) & 0 \\ 0 & 0 & 1 \end{bmatrix}. \tag{3.3}$$

Combining these three matrices represents the full 3 dimensional rotation matrix R_{ij}:

$$R_{ij} = R_z * R_y * R_x = \begin{bmatrix} R_{11} & R_{12} & R_{13} \\ R_{21} & R_{22} & R_{23} \\ R_{31} & R_{32} & R_{33} \end{bmatrix}, \tag{3.4}$$

where each element represents the projection of the jth element of the rotated coordinate system onto the ith element of the lab coordinate system. For a rwUAS in flight and maintaining a fixed horizontal location, it will tilt into any oncoming winds so as to divert some thrust proportional to the speed of the wind. Based on the geometry of this coordinate system, the inclination (vertical tilt) angle ψ is calculated as:

$$\psi = \arccos(R_{33}), \tag{3.5}$$

which is related to the drag force F_d by:

$$F_d = g\ m\ \tan(\psi), \tag{3.6}$$

where g is the acceleration due to gravity, and m is the mass of the platform. Neumann and Bartholmai (2015) suggest that wind speed can therefore be estimated using the definition of drag coefficient c_d:

$$v = \sqrt{\frac{2F_d}{\rho A_{proj} c_d}}, \tag{3.7}$$

where A_{proj} is the projected surface area and ρ is the air density. However, A_{proj} and c_d are generally not known and must be determined, usually as a function of inclination angle using 3D-CAD software. These parameters are also proportional to the angle of attack relative to the platform, which can be complex for asymmetrical designs. Maintaining its dependence on $\sqrt{\tan(\psi)}$, wind speed can be estimated using a simple linear regression model that implicitly accounts for the design factors of the UAV:

$$v = C_0 + C_1 * \sqrt{\tan(\psi)}, \tag{3.8}$$

where C_0 and C_1 are empirically derived coefficients based on comparisons with a reference anemometer (outlined in Section 3.1).

Wind direction can be calculated directly based on the UAV's tilt direction. Accounting for the meteorological definition of wind direction, mathematical definitions of trigonometric functions, and the UAV's coordinate system, wind direction is evaluated simply:

$$\text{direction} = \arctan\left(\frac{R_{23}}{R_{13}}\right). \tag{3.9}$$

3.1.2 Experimental Determination of Coefficients

As stated previously, coefficients C_0 and C_1 from equation 3.8 are functions of the acceleration due to Earth's gravity and other design factors of the UAV such as its mass, surface area, drag coefficient, and motor thrust. These are in turn dependent on the wind direction relative to the UAV's orientation. While there are methods

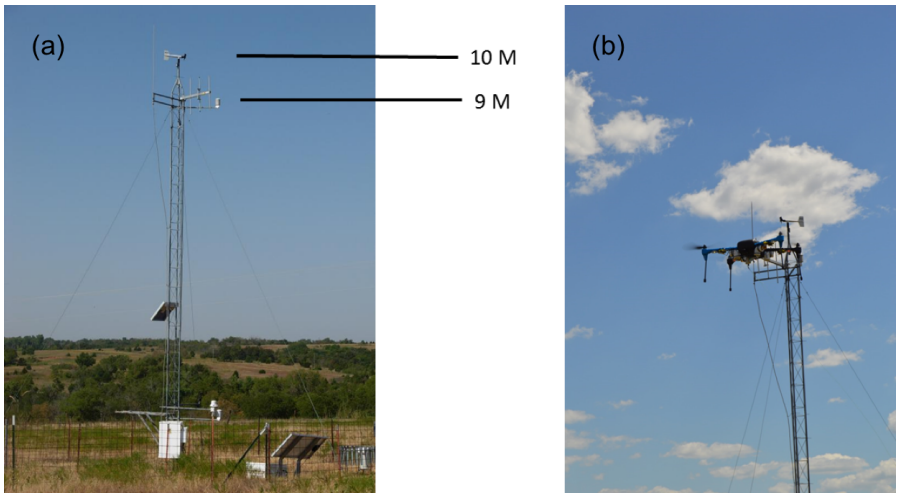

Figure 3.2: Experimental setup for wind vector measurement calibrations. (a) Oklahoma Mesonet towers are outfitted with a propeller vane anemometer at 10 m and measure temperature at 9 m. (b) The Iris+ hovering at 10 m next to the tower, which was performed multiple times over the course of multiple days to gather a large sample of wind speeds and directions. This identical process was also performed with the CopterSonde, maintaining a constant yaw angle so as to account for differing wind attack angles relative to the UAV.

of determining these coefficients in an ideal sense, another approach at estimating them empirically is applied in this study.

Using the Washington, Oklahoma Mesonet tower as a reference (Figure 3.2a), the CopterSonde was flown at a fixed altitude of 10 m directly adjacent to the tower (similar to the Iris+ in Figure 3.2b). The CopterSonde hovered in place for 10–15 min (battery life permitting) at a time. By repeating this process on multiple days with varying wind conditions, a statistical model relating the CopterSonde attitude angles to the real wind vector was calibrated across a representative range. This model assumes the form of equations 3.8 and 3.9, whose coefficients were determined through linear regression of the UAV's autopilot data versus the reference tower. Since the Mesonet averaged observations over 1 min intervals but the

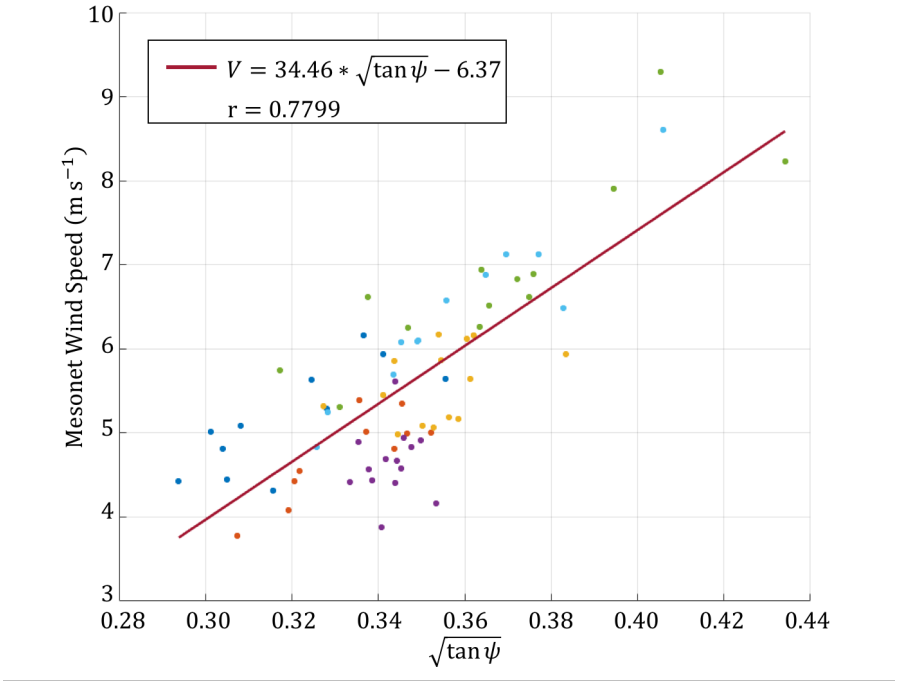

Figure 3.3: Relationship between 1 min averaged wind speed measured by the Washington Mesonet tower to the square root of the tangent of the vertical tilt angle on the CopterSonde. The solid red line denotes the least squares linear fit, which has a correlation coefficient of 0.7799. Data points are colored according to the flight when they were collected.

Pixhawk IMU can measure attitude information at over 10 Hz, the attitude angles were averaged to be consistent with the Mesonet data. While this method smooths out higher frequency oscillations from wind gusts and vibrations, the underlying linear relationship between wind speed and vertical tilt angle ψ is preserved (Figure 3.3). Employing the resulting linear regression model for wind speed (Figure 3.4a) yields root mean square errors of 0.67 m s^{-1}, which is larger than the 0.5 m s^{-1} desired by NOAA (2.1). However, this is likely biased high by a few outlier points at higher wind speeds.

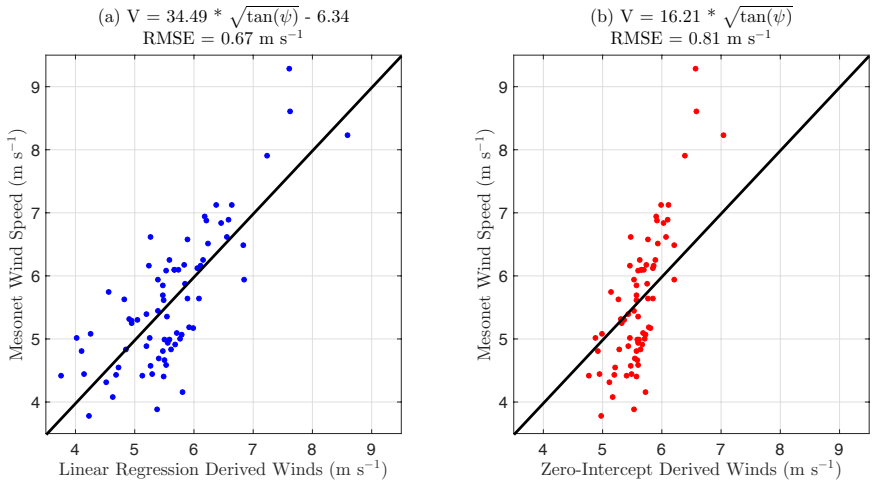

Figure 3.4: Wind speeds estimated in two different manners with respect to the reference 1-minute averaged Mesonet values. (a) Simple linear regression of $\sqrt{\tan(\psi)}$ yields root mean squared errors of 0.67 m s^{-1}, close to the standard requested by NOAA. (b) Linear fit with an intercept forced through the origin as an approximation of equation 3.10. This method increases RMSE relative to simple linear regression, but has a more physical relationship.

Low wind speeds are particularly difficult to measure using a rwUAS, as tilt angles compensating for the wind become negligible and become lost in natural high frequency oscillations. This problem appears in the linear fit as a negative intercept, which implies negative wind speeds for small tilt angles. The theoretical relationship between wind speed and inclination angle ψ given in equations 3.7 and 3.6 described by Neumann and Bartholmai (2015) can be rearranged to read as:

$$v = C\sqrt{\tan(\psi)}, \tag{3.10}$$

where C is the collection of theoretical constants:

$$C = \sqrt{\frac{2gm}{\rho A_{proj} c_d}}. \tag{3.11}$$

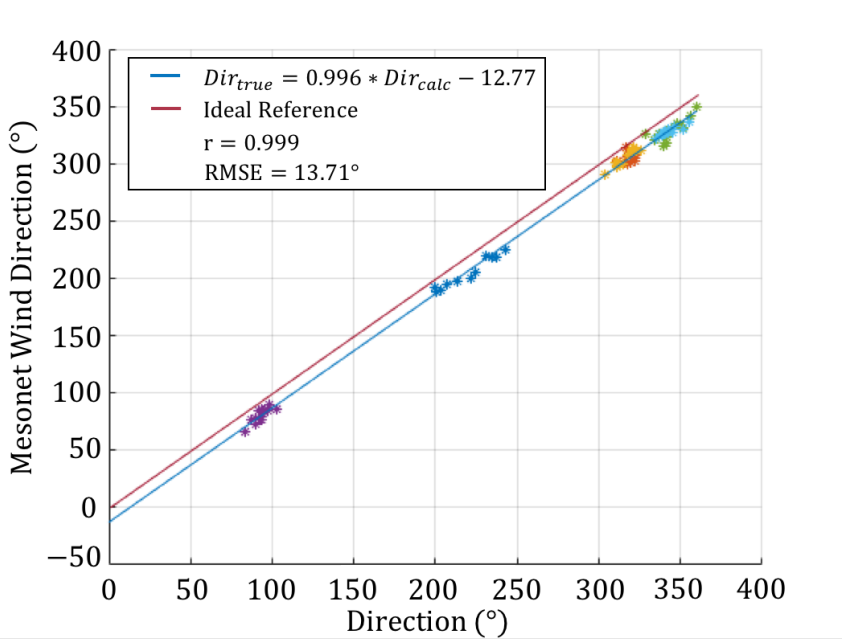

Figure 3.5: Estimated wind directions fit with simple linear regression (blue) compared to the ideal 1:1 line (red). A slope of 0.996 and correlation coefficient of 0.999 imply a significantly linear relationship, but a negative 12.77 intercept skews RMSE to almost 14°. This offset can likely be attributed to magnetometer interference from being in proximity to the metal Mesonet tower, which biases compass headings and therefore wind direction measurements. Otherwise, when averaged to 1-min samples, this estimation method appears robust.

In this sense, instead of dynamically calculating the drag coefficient c_d and projected surface area A_{proj}, one can empirically derive a value for the coefficient C. This results in a similar approach to the least squares fit above, except forcing the intercept to go through the origin (Figure 3.4b). While this makes more physical sense for applications at lower wind speeds and adheres more closely to the theoretical model, the fit derived in this manner results in root mean squared errors of over 0.81 m s^{-1}, an increase of 20% over the least squares regression. For operational estimations of wind speeds, it was decided that the linear regression fit was

the optimal choice because of its higher accuracy. Wind speeds below a certain threshold were therefore filtered out as undetermined measurements.

Equation 3.9 implies that estimating wind direction requires only the direction of tilt, which is independent of wind speed. Fitting results of the CopterSonde flights to a linear regression (Figure 3.5) indicate that this model is appropriate. A slope and correlation coefficient both near unity imply a strong linear relationship, but the 12.77° intercept causes root mean squared errors to appreciably exceed the NOAA guidelines. After further manual field testing, it was determined that this offset was likely caused by the CopterSonde's onboard compass magnetometer erroneously reporting its heading when in proximity to the large metal Mesonet tower. This deviation in yaw angle was consistent across flights on different days due in part by flying in the same location at the same heading each time. With these results in consideration, the estimated CopterSonde wind directions were taken as calculated in equation 3.9 without any linear fit applied.

3.2 Mesonet Environmental Chamber

As discussed in Section 2.4, the iMet sensors were chosen to integrate with the CopterSonde for streamlined data communications. They are advertised to be within the NOAA specifications, but an independent calibration was performed to ensure their robustness. This calibration was conducted on four iMet-XF thermistors in an environmentally controlled chamber operated by the Oklahoma Mesonet. Over a period of 14 hrs, the chamber temperatures were incremented by steps of 10°C ranging between -40 and +60°C (Figure 3.6). A linear bias as a function of temperature range for each sensor was determined by averaging the deviation of each sensor from the chamber's reference probe over 20°C bins (Figure 3.7). The ramp input of the temperature changes was slow enough such that the bias correction also accounts for errors due to response time, so averaging over the whole

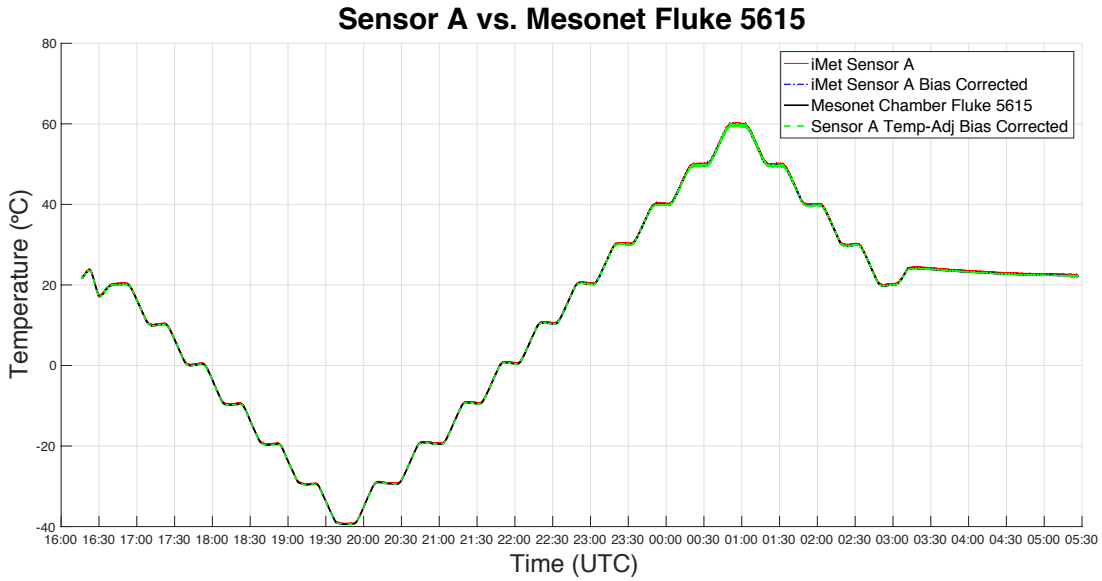

Figure 3.6: Time series of iMet sensor A over course of calibration in environmentally controlled chamber. Temperatures ranged from -40 to +60°C over the course of about 14 hrs.

time period is an adequate approximation. At worst, sensor A exhibits biases of 0.4°C in environments above 40°C, which is within the advertised specifications. However, this sensor trends outside the spread of sensors B–D over the calibration range. When excluding sensor A as an outlier, the accuracy is improved significantly to less than 0.2°C. These calibrations have therefore demonstrated that the iMet thermistors meet the expectations desired by NOAA under ideal conditions. The following section will discuss how these sensors perform in a more realistic environment.

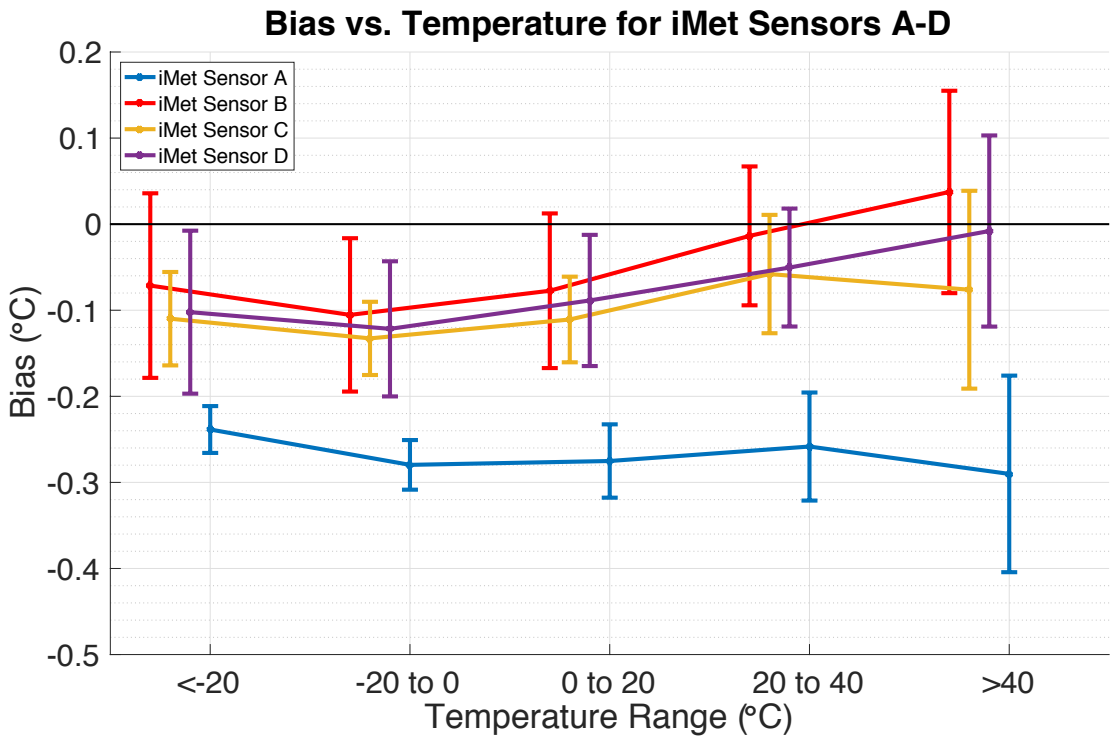

Figure 3.7: Calibration of 4 different iMet sensors.

3.3 Mesonet Tower

Another calibration technique involved aspirated chambers mounted on the Mesonet tower in the parking lot of the National Weather Center (Figure 3.8). These chambers provided reference measurements averaged over one min, and experimental sensors could be mounted inside of them for several hours at a time. While not as robust as using the environmentally controlled chamber, the tower offered a convenient and quick method of obtaining offsets for both temperature and humidity sensors in realistic environmental conditions. This is an important step in maintenance of a thermodynamic sensor package, as normal use on a UAV can cause their responses to drift over time. An example set of these measurements taken in May 2017 for a suite of thermodynamic sensors is shown in Table 3.1.

Figure 3.8: (a) The Mesonet tower in the parking lot of the National Weather Center in Norman, Oklahoma. (b) Mounted on the tower are two aspirated chambers as reference in calibrating the iMet temperature and humidity sensors.

Table 3.1: Summary of average iMet temperature and relative humidity sensor biases compared to NWC Mesonet tower measured in May 2017.

Thermistor ID	Offset (°C)	Humidity ID	Offset (%)
45361	-0.163	0x10A	+3.64
45363	-0.077	0x11A	+3.79
45364	+0.029	0x12A	+3.58
48620	+0.141	0x13A	+3.43
48621	+0.098	0x10B	+3.73
48622	+0.149	0x11B	+3.43
48623	+0.184	0x12B	+2.98
48624	+0.081	0x13B	+3.76
48625	+0.145		
48626	+0.188		
48727	+0.158		
48728	+0.231		

Chapter 4

Sensor Placement

One of the primary functions of the CopterSonde was to collect observations of the PBL in vertical profiles. However, when making measurements, the platform itself can influence these observations. There are a number of factors that can affect any single measurement and each observation must be carefully designed and examined to ensure that external influences are minimized. In this study, we focus on the effects of sensor placement on temperature observations.

To ensure that a thermometer, such as a thermistor, produces accurate measurements, it is critical that the sensor be shielded from solar radiation and properly aspirated with the ambient environment (Tanner et al., 1996; Richardson et al., 1999; Hubbard et al., 2004). Moreover, sensor self-heating can lead to significant measurement bias in some thermistors if not properly accounted for. Thermistors use a temperature-sensitive resistor to measure temperature. By knowing the input voltage and measuring how it changes across the thermistor, the resistance of the temperature sensitive resistor can be determined, and thus the temperature. If current is run constantly through the resistor, heat is generated. Such a sensor must be properly aspirated or the resultant heat can modify the ambient environment, thereby influencing the measurement itself.

Observations of temperature from tower-mounted thermistors typically utilize solar-shielded chambers with fans to mechanically aspirate the sensors to improve

data quality (Brock et al., 1995; McPherson et al., 2007). However, when considering the integration of sensors into a rwUAS, utilizing a fan poses a dilemma. Although a fan could ensure proper aspiration, it would draw power and add weight to the platform and potentially significantly decrease flight duration. Therefore, an alternative solution to this problem is to aspirate the sensors with the air currents produced by the rotating propellers, or rotor wash. However, due to the complex flow around a rwUAS in flight, the location on the rwUAS providing the best aspiration is not obvious. If exposed to too little airflow, the sensor could self heat or not adequately sample the ambient atmosphere. If exposed to too much airflow, compressional heating of the air stream becomes an issue (Rodert, 1941). Furthermore, dissipation of heat from the rotary motor can also alter the measured air. Flow in proximity to the propeller tips is also associated with the highest values of turbulent intensity and temperature fluctuations (Swean and Schetz, 1979). After initial experiments involving rwUAS for research efforts, it was determined that a more in-depth examination of sensor location was needed to ensure data quality.

4.1 Equipment

With the questions surrounding temperature sensor placement on a rwUAS, an experiment was created to objectively determine the optimal location for quality temperature measurements. A summary of the findings from the experiment are discussed below.

4.1.1 Rotary-wing Aircraft and Sensors

As the CASS prototype platform, the CopterSonde (Section 2.3) was chosen for this experiment. Although manufactured to customized standards, results from this study are still directly applicable to other platforms. The CopterSonde was

equipped with iMet thermistors (Section 2.4) that were mounted onto a linear actuator arm which varied their position inside of the propeller wake, as will be described in Section 4.1.4. These sensors were validated in the aspirated shelter at the NWC Mesonet tower prior to these tests, as described in Section 3.3. The CopterSonde was slightly modified from normal operational use: its speed controllers were bypassed so that the speed of the motors were directly proportional to the throttle level coming from the radio transmitter. Since the experiments were performed inside with the aircraft stationary and mounted to a pedestal, this setup allowed for more direct control of the motors instead of allowing them to automatically compensate for the lack of flight.

4.1.2 NSSL Mobile Mesonet

To provide a comparison with the temperature data recorded using the iMet thermistors, a modified version of the National Severe Storms Laboratory (NSSL) Mobile Mesonet (MM) rack was used. The equipment rack, normally mounted to the roof of a vehicle, is capable of temperature, pressure, wind speed and direction, relative humidity, and solar radiation observations. For the tests presented here, the equipment rack was mounted to a cart. This allowed the rack to be placed in close proximity to the CopterSonde during measurements.

To measure temperature, two Campbell Scientfic model 109 thermistors (CS 109) were used. One was mounted inside an aspirated radiation shield and one was mounted to the CopterSonde. The 109 probe has less than 0.03°C linearization error over the range of -50 to +70°C, with a ±0.2°C tolerance between 0 and 70°C. The thermistor is contained within a stainless steel housing, meant for use in damp conditions such as soil moisture measurements, and as such has a response time of 30 s with 5 m s^{-1} airflow. The sensors used for this study had been recently calibrated in the Oklahoma Mesonet calibration lab to ensure their accuracies.

4.1.3 Oklahoma Mesonet hot wire anemometer

In addition to measuring temperature, it is also relevant to measure the flow rate at the temperature sensor location. This allows one to assess the extent to which the probes are in a "well mixed" environment and provides insight to the conditions that are being experienced by the sensors themselves. A Thermo Systems Inc. (TSI) hot-wire anemometer was used to gather precise velocity measurements as close as possible to the temperature sensor mounting locations.

4.1.4 Linear actuator arm

The overall goal of the experiment was to find locations on a rwUAS where temperature readings are most representative of the environment. With this in mind, data collected at multiple locations on the rwUAS were examined to determine where the sensors experience bias relative to ambient air. To achieve this, the thermistors were placed on a linear actuator arm which moved the sensors horizontally directly underneath two of the motor mounts (Figure 4.1). The initial starting position at point A was 6.5 cm outside of one propeller, and the the sensor position was stepped by 0.24 cm with a dwelling time of two seconds per increment across the width of the CopterSonde towards point B. The ground station recorded arm position, wind speeds, and computer timestamps at each step. The ending location was 12.5 cm outside the opposite side of the rwUAS, and took approximately 35 min to complete the process. Two of the iMet temperature sensors were attached to the arm, as was a 109 temperature sensor from the NSSL MM rack. Combining these three different datasets (NSSL logs for the NSSL probes, Pixhawk logs for the temperature sensors, and the computer logs for the arm and the anemometer) with their common timestamps therefore allowed for synchronized analysis of the separate data streams.

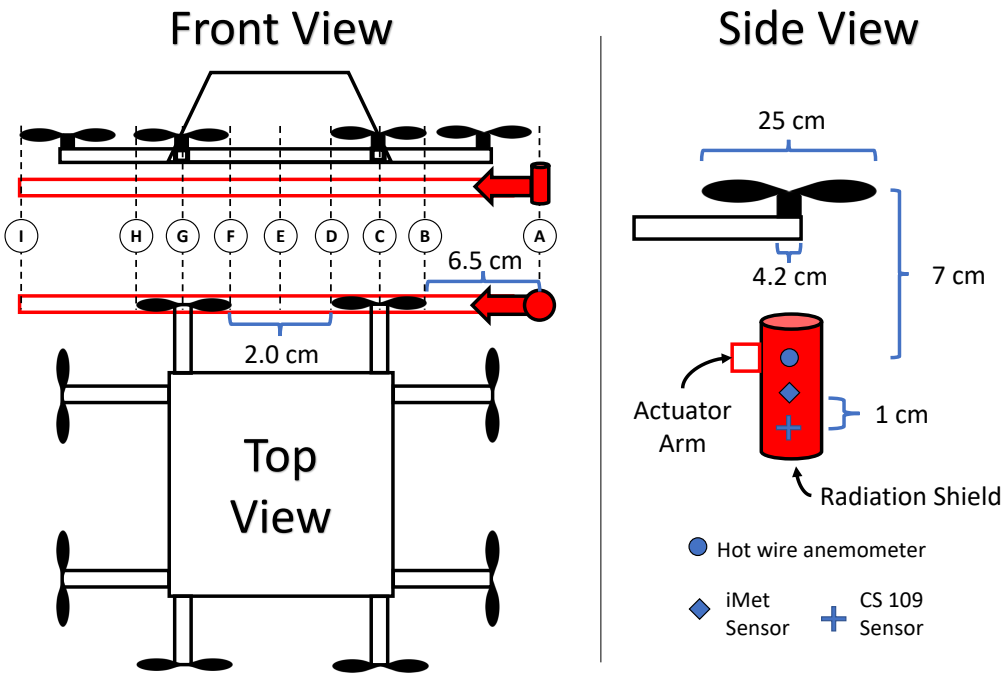

Figure 4.1: Schematic and dimensions of the rwUAS used in this study (drawing not to scale). In front and top view, the linear actuator arm is represented by the red rectangle outline, and the sensor package as a red circle. The arm was displaced from point A to point I, directly underneath the motor mounts and one pair of propellers as seen in the top-down and side views. Point B represents the tip of propeller 1, point C is directly under motor 1, D is the other side of the same propeller. Point E is halfway between the two propellers, and points F–H are symmetrical to points B–D.

4.2 Thermistor self-heating experiment

Prior to analysis of the sensor placement temperature profiles detailed in later sections, a baseline depiction of the iMet thermistor self-heating is required. A simple experiment consisting of three thermistors and a ducted fan was conducted to isolate the effects of aspiration. The fan was located at the base of a solar shield duct, which was bent at a right angle with sensors inserted through holes along the top. With the fan switched on, this configuration induced airflow to enter horizontally, pass across the sensors, and exhaust downwards through the fan.

The sensors were initially powered on to collect data while the fan was off. After holding this condition for approximately 6 min, the fan was powered on, pulling air across the sensors at 6 m s^{-1}. The fan was then alternately switched on and off for periods of two to three minutes each, for a total of three cycles.

Analysis of the iMet temperature responses (Figure 4.2) revealed that the sensors closely tracked with one another while the fan was on, with only a linear offset. It is immediately apparent that the sensors react to airflow through the solar shield, as temperatures repeatedly drop over 1°C in under 20 s. Prior to the first time the fan was switched on, the setup was idle for several minutes. However, following the fan being switched off, the sensors indicated temperature increases. For these periods, the observed heating was likely due to a combination of both sensor-self heating and the fan motor radiating heat upwards towards the sensors. This hypothesis is supported by iMet sensor 2 being in closest proximity to and directly above the fan while also heating the most rapidly. Furthermore, the other two sensors were higher up and displaced horizontally due to the geometry of the duct, and they showed slower heating rates while the fan was off. The key evidence for sensor self-heating is that the sensors return to their same respective temperature levels each time the fan was on, regardless of how they behaved while the fan

was off. Therefore, this supports the requirement of sensor aspiration to properly measure the environmental temperature.

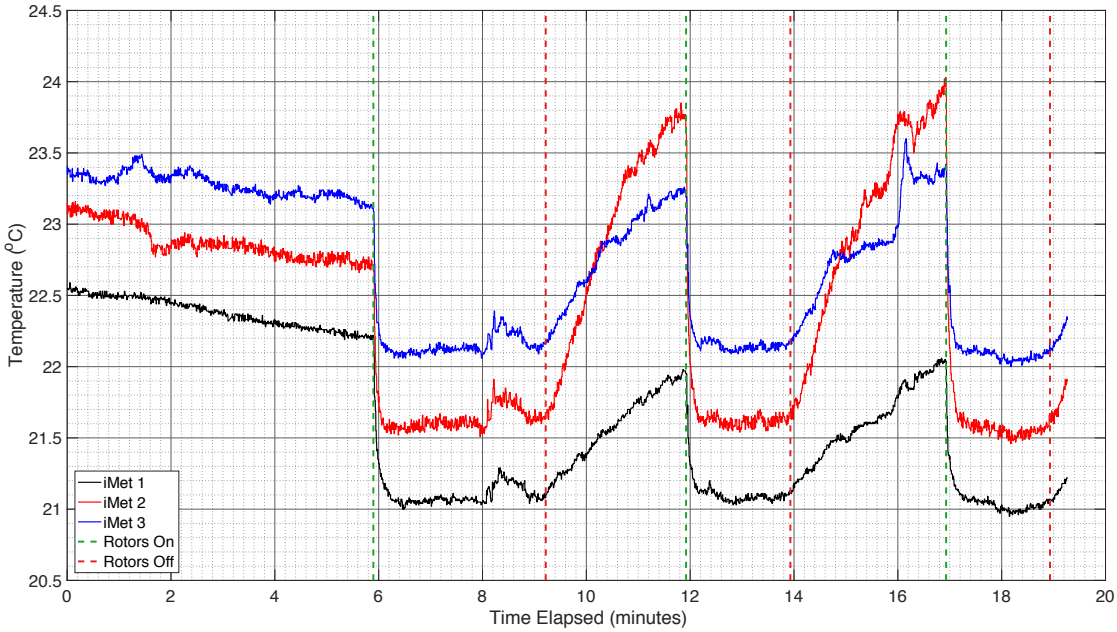

Figure 4.2: Time series of the uncalibrated iMet temperature sensors sampling at 10 Hz relative to the times the fan was switched on (green dashed line) and off (red dashed line).

4.3 Anechoic chamber experiments

4.3.1 Setup

The University of Oklahoma Radar Innovations Laboratory has a large anechoic chamber used for calibration and testing of radar components and other electronic equipment. This chamber however also provides a reasonably homogeneous environment for testing when it is necessary to isolate the effects of various sensor influences on a rwUAS without solar radiation concerns or changes to the ambient environment. To offset the vertical variations in temperature that could exist in

such a room, a common carpet fan was directed at 45° from horizontal and turned on to maximum airflow for about 15 min before the experiment to mix the environmental air. The CopterSonde was mounted on a large pedestal near the center of the room with a bracket that accommodated the vehicle and a linear actuator arm as previously mentioned (Figure 4.3a).

To simulate the wind flow of the aircraft in flight, the iMet and CS 109 thermistors and hot wire anemometer were positioned inside of a 3D-printed plastic solar shield (Figure 4.3b, c). Due to the spatial constraints of the setup, the CS 109 was mounted vertically and underneath the iMet and wind sensors in an effort to measure the same air stream. Furthermore, to avoid bias in temperature measurements, the hot wire anemometer was removed for the final round of testing. For each experiment, the actuator arm was mounted so that the sensors would pass directly underneath the motor mounts as the linear actuator arm moved horizontally (Figure 4.1).

To provide a reference temperature of the ambient environment, a second CS 109 sensor on the NSSL MM rack was mounted inside the aspirated U-tube radiation shield (not depicted, see Waugh and Fredrickson, 2010). A second iMet thermistor was also suspended 50 cm below the CopterSonde, allowing for reasonable (but turbulent) aspiration, as determined from previous trials not included in this study. The additional measurements provided by the suspended iMet thermistor and the CS 109 probe inside the radiation shield, were used to measure the "ambient" environment. For the purposes of these tests, the autopilot inputs to the motor throttle were bypassed, allowing for direct manipulation of throttle input using an external device.

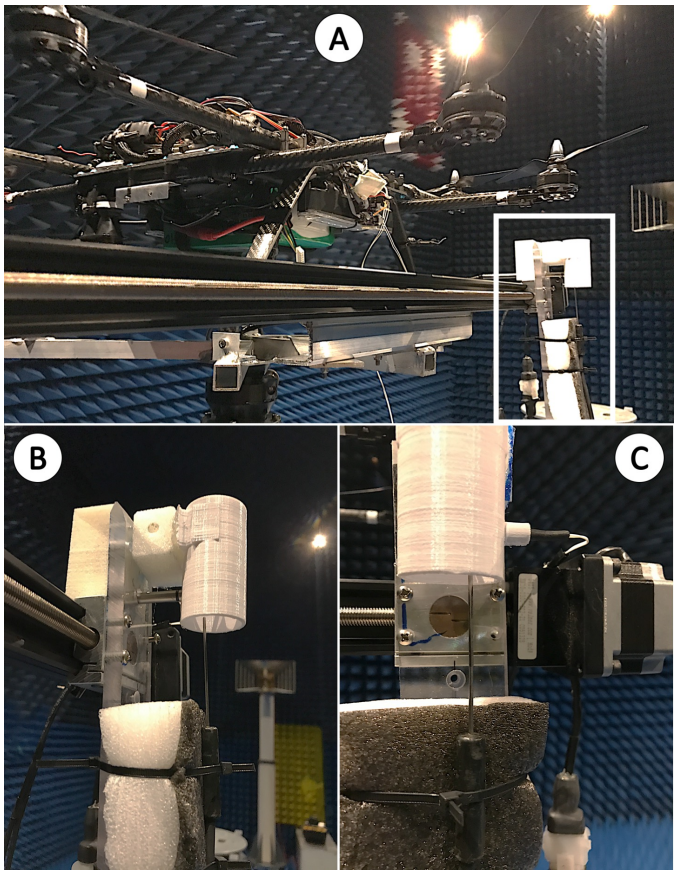

Figure 4.3: A: Position of linear actuator arm underneath rwUAS on mounting pedestal. Arm was aligned such that sensors passed directly underneath the motor mounts so as to make the system essentially two-dimensional. The sensor package is outlined in white. B: Close-up side view of the sensor package. The NSSL thermistor (CS 109) is strapped vertically to a foam mount so that it reaches inside the solar shield (white cylinder) from the bottom. The hot-wire anemometer is attached to the linear actuator arm with a clear mount and passes into a hole on the back side of the solar shield. C: Close-up front view of the sensor package. An iMet thermistor (PT 100) enters the solar shield through a hole on the right side. CS 109 also visible pointing vertically.

4.3.2 Procedure

To begin, power was supplied to the iMet and NSSL thermistors and they began logging data. For the first trial, the motor position began at point A (6.5 cm horizontally from the tip of the nearest propeller, Figure 4.1), and the battery was connected with throttle at zero, allowing the sensors to sample an unaspirated environment for 8 min. After this period, the CopterSonde was throttled up to approximately 55% maximum power to simulate the airflow typical during slow ascent. Although not directly under the propellers, airflow across the sensors was 2 m s^{-1}, sufficient enough for aspiration. This position was sustained for two min before powering the motors off again. The sensors then remained in quiescent conditions for 2.5 min before throttling to 55% again. After giving the sensors 40 s to aspirate, the linear actuator was then incrementally moved towards point B by 0.24 cm, holding each position for 2 s. In total, it moved approximately 71.1 cm, which was outside of the rotor wash on the "B" side of the configuration. This experiment took a total of approximately 35 min to complete.

To control for the effects of potential heat advection from the hot-wire anemometer, the same test was conducted after removing it from the solar shield. During this second trial, however, the initial start-stop-start of the motors was not performed. The CopterSonde and sensors were powered on for 2.7 min, then the throttle was increased to 55% for 35 s before incrementing the linear actuator arm's position.

4.4 Results and discussion

4.4.1 Experiment 1 - wind probe in tube

In the first experiment, to account for the longer response function of the CS 109 probes and to make more appropriate comparisons, a moving 10 s average of the

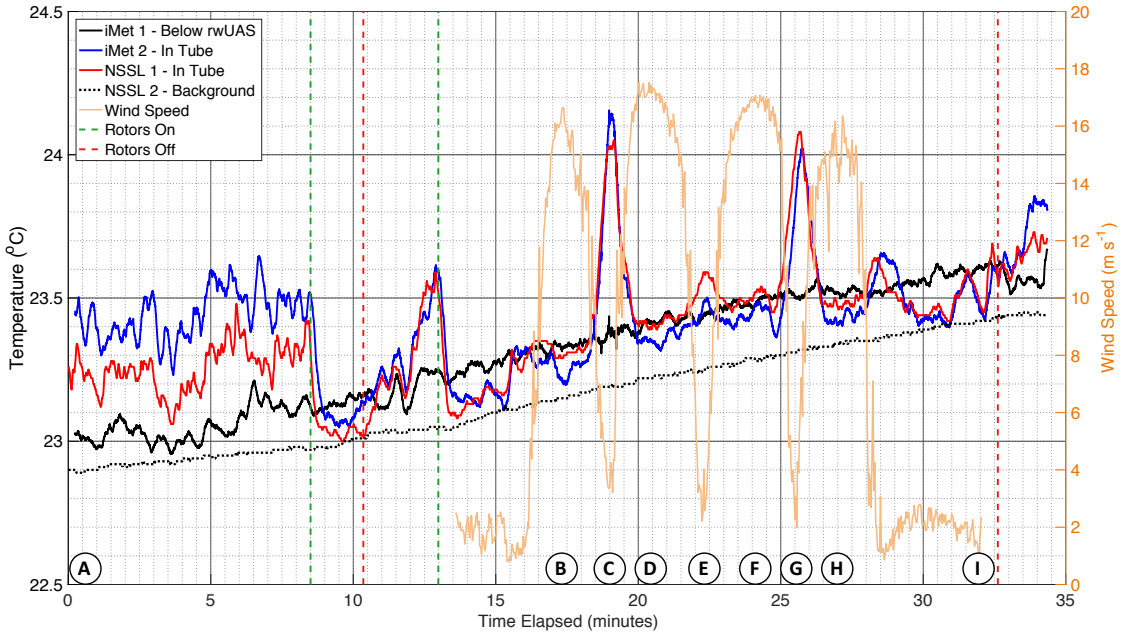

Figure 4.4: Experiment 1 - Time series graph of air temperature (°C) and wind speed (m s^{-1}). The background temperature is shown by the CS 109 probe (dotted black) and the iMet sensor (solid black). The CopterSonde temperatures are shown by the iMet sensor (solid blue), while the reference temperature of the CS 109 is shown in solid red. Air velocity at the CopterSonde sensor location is plotted in solid orange. Dotted green and red vertical lines indicate times when the motors were throttled on and off, respectively. Points A–I from Figure 4.1 are also indicated here.

iMet temperature data was calculated before each analysis point (Figure 4.4). The wind speeds presented are the raw outputs. Furthermore, the hot-wire anemometer had not been calibrated prior to this experiment, and thus values displayed may not be absolute. Confidence in relative precision is still high, however.

The air flow velocity peaked near 17 m s^{-1} before decreasing to near zero directly underneath the motor which clearly identified passage through the rotor wash of the propellers as the linear actuator moves from one side of the rwUAS to the other (Points B, D, figure 4.1). A second minimum was encountered between

the two propellers, before a similar pattern was observed while the sensors passed under the second propeller. A gradual temperature increase of 0.5°C was observed by both background temperature sensors over the course of the 35 min experiment, likely attributable to the mechanical mixing of the chamber environment.

This velocity pattern and associated temperature bias demonstrates that when considering sensor location for adequate airflow, directly under the motors or between the two propellers is not a viable option. While the first conclusion might be obvious, a relative minima in the flow velocity was not expected between the propellers. In addition to the velocity structure, it is also evident that differences do exist between the various sensors, and that a steady increase in temperature on all sensors was measured over the duration of the experiment.

A closer look at the first 16 min of this analysis relative to the background temperature (Figure 4.5) reveals evidence of the self-heating phenomenon. For over 8 min, the probes in the solar shield recorded 0.2–0.4°C above the relatively constant background, with variations owing to the presence of the hot-wire anemometer. During this period, the motors of the CopterSonde were not on, thus no aspiration to the sensor existed. Once the motors initially throttled up, temperatures dropped to within 0.1°C of the reference, and remained in this range until the motors were shut off again 2 min later. Immediately after throttling down, temperature began rising again, by 0.5°C in under 3 min. Finally, when throttled back up again at the 13 min mark, temperatures returned to anomalies of 0.1°C in under 30 s. While wind speeds were not recorded during this time, it is reasonable to extrapolate the 2.5 m s^{-1} reading backwards from min 13.6 since the sensor position was fixed.

Although influences from the anemometer are likely inherent during this initial period, the overall response of the sensors to aspiration matches results from the experiment discussed in Section 4.2. It can therefore be concluded that rotor wash is capable of mitigating the decoupling of sensors from the ambient environment,

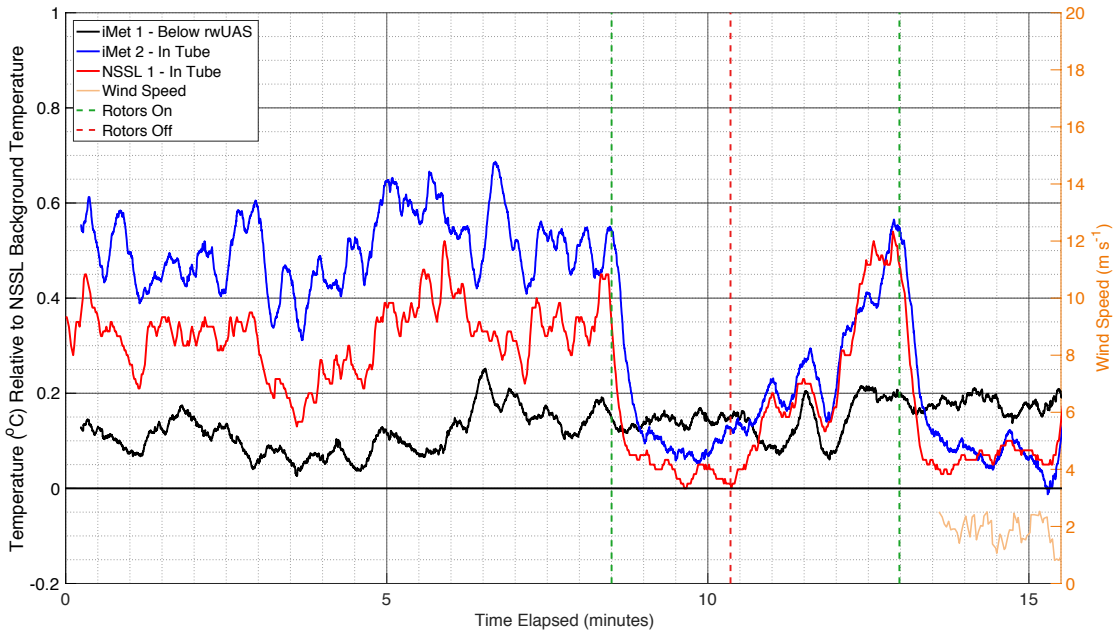

Figure 4.5: Temperatures (°C) relative to NSSL background temperature at the beginning of experiment 1 to reiterate sensor self-heating. Propellers throttling on and off (green and red vertical dashed lines, respectively) seem to directly impact temperature measurements.

so long as the sensors are free from other external sources of heating which will be discussed below.

After the motors turned on at the 13 min mark, the actuator arm began translating underneath the aircraft. Due to the complexity of the flow field underneath propellers rotating at several thousand revolutions per minute, it is reasonable to believe that small nuances in temperature depicted can be caused by limits in sensor accuracy and sampling rates in turbulent flow. There are, however, several identifiable trends that are attributable to artificial sources such as motor heat and sensor decoupling (Figure 4.6).

At min 15.5 (just prior to point B), the probes intercepted a warm stream of air likely owing to turbulent fluctuations and compressional heating on the tip of the propeller spreading down and outward along the periphery of the propeller wash.

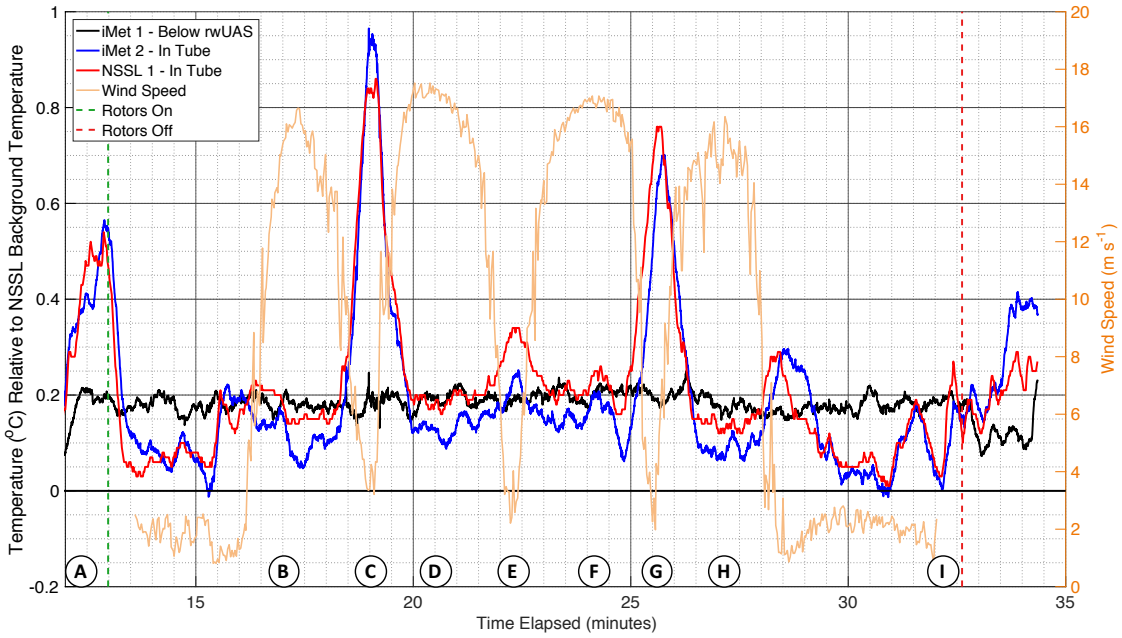

Figure 4.6: Experiment 1 time series of temperature (°C) relative to the NSSL background temperature after the actuator arm begins incrementing. Points A–I are included from Figure 4.1.

A similar observation is made on the other end of the CopterSonde at min 28 (after point H). At min 16 (point B), the sensors moved under the propellers and out of the warm air stream from the tips, allowing temperatures to stabilize within 0.2°C of the reference temperature. This pattern is consistently observed underneath the four peaks in wind speed, representing: exterior propeller 1 (point B), interior propeller 1 (point D), interior propeller 2 (point F), and exterior propeller 2 (point H), in order.

As the actuator arm moved the sensors underneath the CopterSonde's motor mounts from min 18–19.5 (point C) and 25–26.5 (point G), temperatures rapidly rose 0.7–1.0°C relative to the background over the course of 1 minute (Figure 4.6). Since temperatures began rising with wind speeds well above levels at the beginning of the experiment (2–4 m s^{-1}), the source of this increase was not necessarily solely

due to self heating. Instead, their proximity to the motors leads to the conclusion that the sensors were intercepting hot air advected from the motors.

Finally, the sensors mounted on the arm sampled the space in between the interior propeller tips at min 21.5–23 (Point E). At that time, wind speeds dropped to less than 3 m s^{-1}, similar to those at the initial position of the sensors. Subsequently, a small (0.1°C) temperature rise is noted in both the iMet and NSSL sensors. Because the aspiration rates were similar to those at the beginning of this experiment, the primary driver of this temperature rise was likely a warm air stream originating from the hot wire anemometer. In order to remove this effect, a second analogous experiment was performed by removing it.

4.4.2 Experiment 2 - no wind probe

In Experiment 2, sensors were allowed to remain unaspirated for about 2.75 min before throttling up and moving the linear actuator arm, similar to Experiment 1 except without the initial aspiration test. Although the wind probe was removed, the actuator arm increments were identical, so it is reasonable to compare the temperature time series against the wind speeds from Experiment 1 (Figure 4.7). In general, the temperature pattern was largely similar to the results from Experiment 1: symmetrical about the center of the two propellers, increases in temperature on the outside tips (before point B and after point H), and large increases underneath the motor mounts (points C and G). However, the small rise in temperature in between both propellers (point E) was no longer observed, and the overall increase in temperature underneath the motor mounts was 0.2–0.3°C less than in Experiment 1. Therefore, the hot-wire anemometer likely biased temperature readings in this region of relatively stagnant flow. Finally, the CopterSonde's battery rapidly approached its critical level as the motors were shut off at min 18.5, so temperature trends after this mark should not be strongly considered.

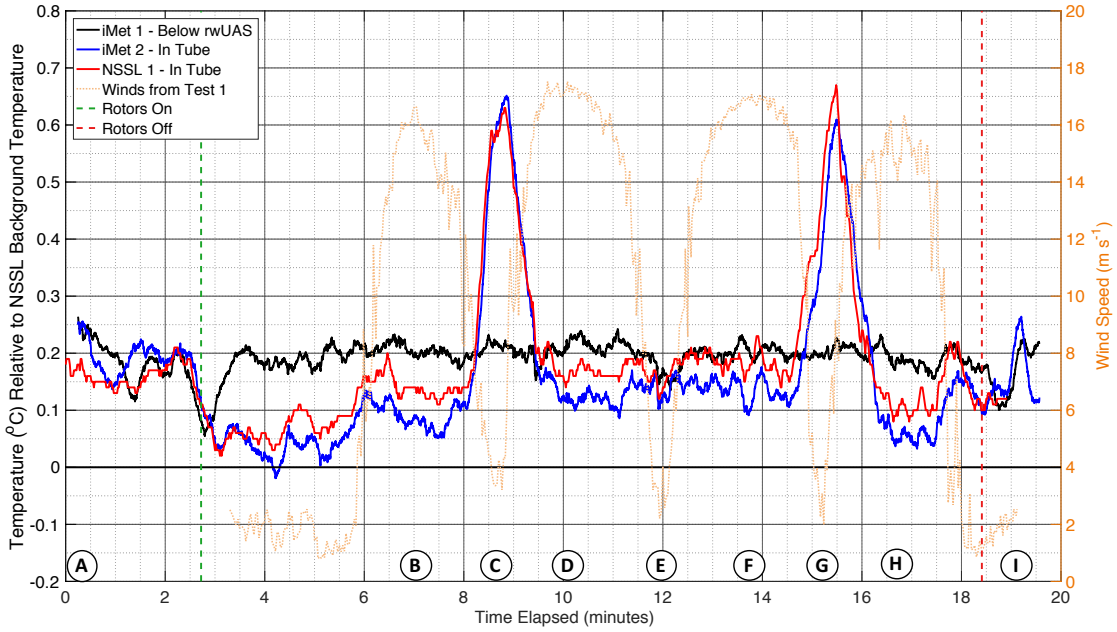

Figure 4.7: Experiment 2 - temperature and wind speed vs. relative time. Winds from Experiment 1 included for reference (dotted orange). Letters A–I included from Figure 4.1.

Chapter 5

Field Validation

In Chapter 2, the CopterSonde was introduced as a method of collecting lower atmospheric observations using an iMet thermodynamic sensor package. These sensors were calibrated and determined to be robust (Sections 3.2 and 3.3), and careful consideration was taken in determining their location on the CopterSonde (Chapter 4). Furthermore, a method of estimating wind speeds from the UAV tilt was evaluated and produced encouraging results (Section 3.1). With these successes in the design and calibration phases, the next step in development involved collecting environmental observations with scientific objectives to validate the measurements against other sources. Through this method, one can determine whether CopterSonde measurements reflect systematic errors or if they accurately represent the environment.

One of the first opportunities to test the capabilities of the CopterSonde came with the EPIC field campaign, supported by the NOAA UAS office and led by the National Severe Storms Lab (NSSL) in May 2017. NSSL and OU, in conjunction with the University of Colorado Boulder (CU) and the Swiss company Meteomatics, Inc., aimed to evaluate the capability of UAS to provide valuable lower atmospheric observations in pre-convective environments for use by forecasters at the National Weather Service (NWS). Combining expertise in disciplines across engineering and meteorology, this collaboration also sought to raise the "technology

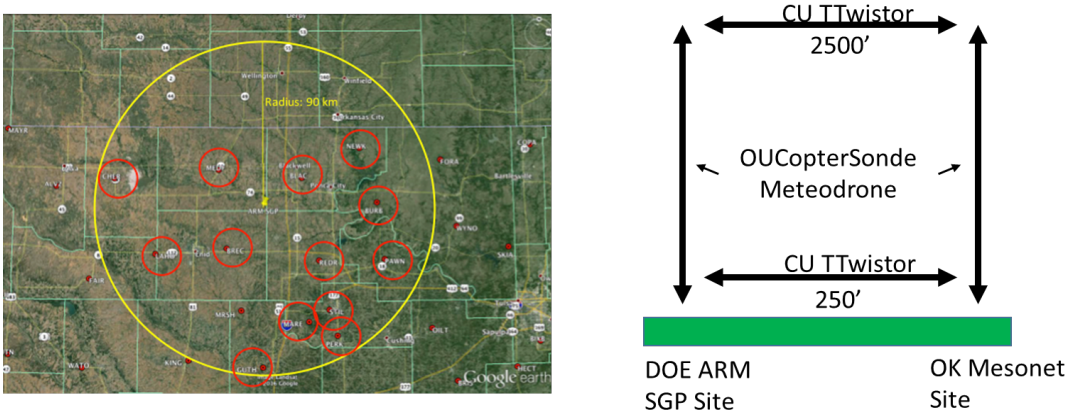

Figure 5.1: Concept of operations for the EPIC field campaign in May of 2017. The DOE ARM SGP site in Lamont, Oklahoma (center of yellow circle) was selected as the base of operations due to its vast array of atmospheric monitoring equipment. Oklahoma Mesonet locations (red circles) were selected based on weather forecasts for each day, and vertical profiles were performed at the SGP and selected Mesonet sites by the OU CopterSonde and Meteomatics Meteodrone rwUAS. In the meantime, the CU TTwistor fwUAS flew horizontal transects between the two locations. Flights to 2500 feet AGL were permitted within the red circles in proximity to the Mesonet sites.

readiness level (TRL)" of the UAS capabilities through refined PBL measurement strategies, quantification of measurement uncertainties, and communication of the unique observations in near-real time. The details of this project and its results will be discussed in the following sections.

5.1 EPIC Concept of Operations

Temperature, moisture, and momentum distributions within the PBL can strongly dictate the potential for severe storm development. By utilizing high-resolution measurements from UAS, EPIC sought to explore their potential to measure the

Figure 5.2: CU TTwistor launching from the roof of a chase vehicle (left). The Meteomatics Meteodrone hexcopter (right). These platforms, along with the OU CopterSonde, were the primary methods of sampling the PBL during EPIC.

rapidly changing fields of moisture, instability, and vertical wind shear not resolvable by traditional observational networks (e.g., Koch et al., 2016). A domain encompassing north-central Oklahoma in mid-May was chosen as a target for operations, which were centered upon the Department of Energy (DOE) Atmospheric Radiation Measurment (ARM) Southern Great Plains (SGP) facility in Lamont, Oklahoma (Figure 5.1). The SGP site is outfitted extensive atmospheric observational systems, which was utilized for UAS measurement validation in October 2016, prior to the main campaign. The aircraft in this campaign consisted of the OU CopterSonde (discussed earlier), the CU TTwistor (a fwUAS capable of several hours of flight; Houston et al., 2012), and the Meteomatics Meteodrone (a lightweight rwUAS; Figure 5.2). Special flight permissions from the FAA were granted for these platforms to fly to an altitude of 2500 ft (760 m) AGL within visual line of sight at specific Mesonet locations (Figure 5.1). Unfortunately, the permissions to fly at this altitude at the SGP were not granted in time for the field campaign, so flights were primarily conducted at Mesonet sites.

Each day, the NWS in Norman, Oklahoma, provided a weather briefing in support of determining potential convective initiation. Having knowledge of forecasted mesoscale airmass boundaries (fronts, dryline, outflows, etc.) for the day, two Oklahoma Mesonet sites were then chosen in an effort to transect the feature in question (Figure 5.1). Teams consisting of one CopterSonde and one Meteodrone were deployed to the selected Mesonet sites to perform continuous vertical profiles while the TTwistor flew horizontal transects between the two. This setup allowed for monitoring of both spatial and temporal heterogeneities in the CBL. For further validation of the vertically profiling rwUAS, radiosondes were also launched at regular intervals at the two sites from an NSSL mobile mesonet (Straka et al., 1996) and the Collaborative Lower Atmospheric Mobile Profiling System (CLAMPS), a mobile platform consisting of a Doppler lidar, atmospheric emitted radiance interferometer, and microwave radiometer.

Flight teams required several personnel assigned to specific roles in accordance with the special FAA requirements. Four roles were required: 1) a licensed private pilot served as the pilot in command (PIC) to communicate with other air traffic and surrounding control towers, 2) a visual observer with FAA class II medical qualifications was tasked with monitoring the sky to avoid in-air collisions, 3) someone with experience flying UAVs was in charge of the radio transmitter to take over in case of an emergency, and 4) a person monitored the ground station for data quality and relay information about the aircraft's performance while in flight. With all of these safety precautions in place, vertical profiles were acquired by alternating CopterSonde and Meteodrone flights once every 15–20 minutes, and continuous TTwistor transects flown until the onset of storms made flight conditions unsafe, signaling the end of operations for the day.

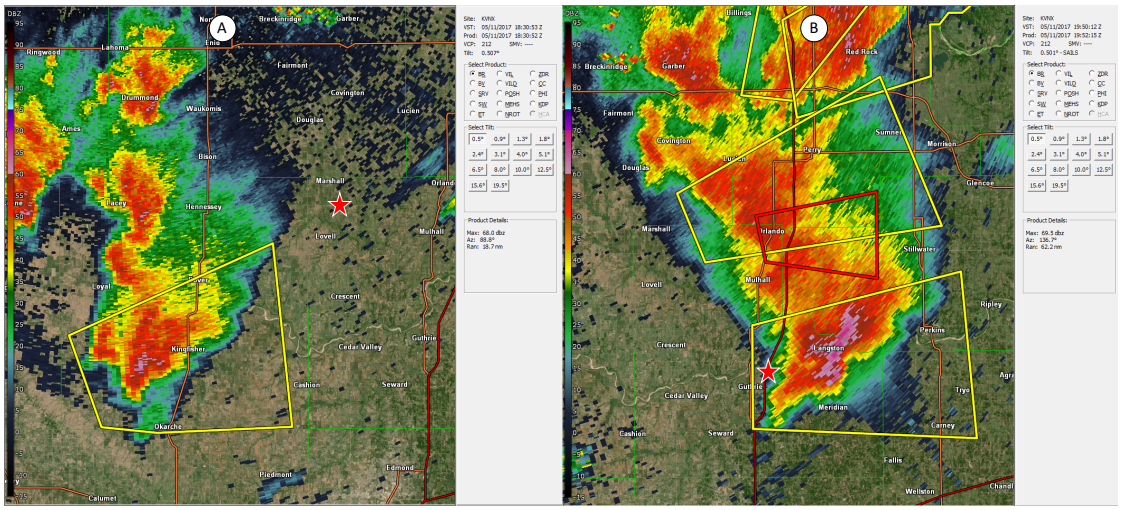

Figure 5.3: Doppler radar reflectivity factor image from KVNX on 11 May 2017. The red start denotes the approximate location of the OU profiling team at each time. A: at 1830 UTC, the storm was severe-warned and was drawing inflow from the region sampled during the campaign. B: after sampling teams had ceased operations, the storm eventually produced a tornado as it passed the I-35 corridor.

5.2 11 May 2017 Case Study

On the afternoon of 11 May 2017, the OU team deployed to the Oklahoma Mesonet site in Marshall. While flying vertical profiles with the CopterSonde, a thunderstorm initiated to the southwest of the site which shortly thereafter developed a mesocyclone and became severe-warned (Figure 5.3A). At this point, the team ceased operations for the day, and narrowly missed intercepting the storm as it went on to produce a confirmed tornado near Orlando (Figure 5.3B). While taking measurements, it was visually apparent from the Mesonet tower that the winds at the Marshall site had transitioned from northwesterly background flow to more northeasterly as the storm grew in intensity and began drawing in air from its northeast. The winds estimated from the CopterSonde (Figure 5.4) agree with this observation, indicating that the environment sampled at the Marshall site was

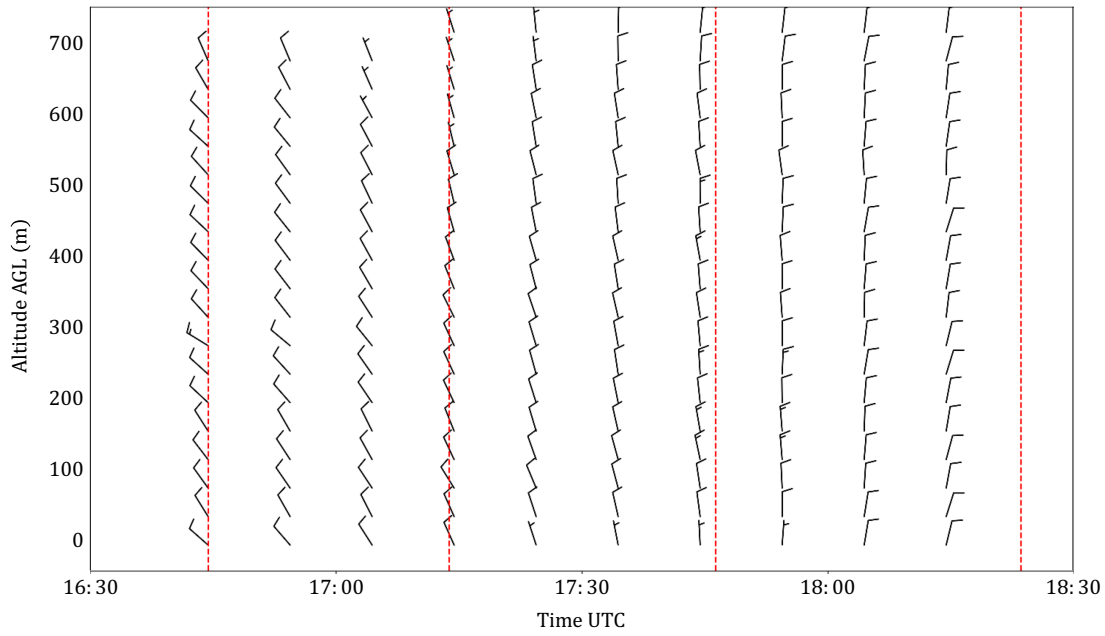

Figure 5.4: Time-height coordinates of horizontal winds (in knots) estimated by the CopterSonde at the Marshall Mesonet site on 11 May 2018. The winds change from northwesterly background flow to northeasterly storm inflow over the course of about 90 minutes as a severe thunderstorm begins modifying its environment.

being directly ingested into the pre-tornadic storm. With this information being communicated back to forecasters in Norman in real time, this case demonstrates the utility of UAVs being deployed in a near-storm environment.

5.3 Results and Summary

Over the two-week period of the primary field campaign, observations were collected in several pre-convective environments. These deployments included sampling the inflow region of a pre-tornadic supercell (11 May 2017) and the warm sector of a remarkably volatile environment forecasted by the Storm Prediction Center (SPC) to be of highest risk for severe weather (18 May 2017). One of the

largest achievements of the campaign for OU and CASS was the significant improvement in TRL of the CopterSonde. Compared to test flights just a few months prior, experience gained during EPIC streamlined operations considerably. A more comprehensive pre-flight safety checklist was developed. Novel autopilot programming and integration with the ground station allowed for onboard pre-flight preparations, simplifying the process to begin data collection. Communication skills between the flight team members and coordination between other teams became crucial for successful flights, and team members became familiar with their responsibilities while grounded such as charging batteries and post-processing data for upload. Weaknesses in platform and software design were diagnosed and addressed at the end of each day, leading to a more robust system with each iteration.

In addition to having a reliable aircraft for atmospheric measurements, this logistical side of operations was a key component in assessing the overall capability of UAVs to fill the data gap in the PBL. While many aspects of the EPIC campaign proved successful, this was still the first true test of the CopterSonde's abilities and was not without room for improvement. For example, the areas with special permission to fly above the general 400 feet AGL limit in uncontrolled airspace was extremely limited relative to the coverage of typical convective development. Having access to Mesonet sites was certainly beneficial, but many of the weather systems in the time period were outside of the domain of interest. The primary boundary driving the high risk event on 18 May was several hundred kilometers away from the closest site with special flight access, significantly impeding the capability to transect it. In its current state of regulations, being able to fly high enough to collect the necessary data can often come down to whether a storm develops and propagates close enough to a predetermined flight area. Nonetheless, these regulations were strictly obeyed during operations, as they existed to keep the airspace safe.

In addition to airspace limitations, data quality were occasionally affected by CopterSonde performance issues. Being of symmetrical design with a square plate in the center, the CopterSonde was largely susceptible to harmonic vibrations when in flight. These vibrations could occasionally be significant, and affected the representativeness of measurements collected. Furthermore, it was discovered that sensors required their own separate power source isolated from the main battery driving the motors since they required a clean, consistent current draw to maintain smooth measurements. These problems were addressed shortly after the campaign, which significantly improved the quality of measurements. Even with these shortcomings, the lessons learned and experiences gained during EPIC were instrumental in development of the CopterSonde, elevating it to a reliable platform with robust measurement and deployment capabilities.

Chapter 6

Boundary Layer Transitions

Knowledge of the diurnal cycles of temperature, humidity, and winds in the PBL can significantly improve forecasting skill in the many applications detailed in Section 1.1. Beginning at sunset, land surfaces cool via longwave radiation overnight more rapidly than the atmosphere directly above in the absence of advection and cloud cover. These conditions induce a shallow and stably stratified PBL with minimum surface temperatures occurring directly before sunrise the following morning. Following sunrise, the surface is warmed via incoming shortwave radiation and the low-level temperature inversion is eroded as buoyant surface air parcels act to mix an increasingly deep layer. This continues until the convective boundary layer (CBL) is established. This transition of the temperature profiles has been well documented (e.g., Stull, 1988) and is a fundamental aspect of the PBL.

While traditionally difficult to measure (see Section 1.2), the diurnal transition of the PBL is one of many areas of interest for UAS applications. By continually observing vertical profiles with the CopterSonde (Section 2.3), thermodynamic and kinematic processes involved with the morning PBL transition were examined on multiple occasions. These results will be discussed in the following sections.

6.1 Background

While there are numerous processes that act to physically modify PBL heat and moisture profiles during the morning transition period, one of the main drivers is vertical turbulent sensible and latent heat fluxes. Angevine et al. (2001) described these mechanisms though analysis of meteorological tower and wind profiler data, and concluded that surface layer heating that occurs immediately after sunrise is primarily due to turbulent diffusion from above. This study also developed and validated a finite-difference model to predict surface wind speed and temperatures based on their results. Although this was one of the first studies to document the morning transition, it was limited in vertical extent by surface towers and resolution to which the boundary layer profiler could observe. Lapworth (2006) expanded on the observations of morning PBL transitions by creating a six year summer climatology of measurements obtained with a tethered balloon system in conjunction with a sonic anemometer and platinum resistance thermometer near the surface. These measurements were collected inland on nights with strong radiative cooling followed by morning insolation. Results from these continuous profiles agreed with Angevine et al. (2001) that after sunrise, the surface remained stable such that the initial heating was mainly from downward heat fluxes until the near-surface heat fluxes change from negative to positive. Even after this transition, the layer is warmed mostly due to entrainment from above the nocturnal inversion until the solar radiative flux becomes large enough to drive the convective boundary layer.

Advances in computational abilities in the past several decades have allowed for large eddy simulations (LES) to become a useful tool for evaluating turbulent-scale processes in the PBL. For example, Fedorovich et al. (2004) demonstrated that the convective boundary layer is characterized by positive turbulent heat fluxes near the surface which then decrease aloft and become negative in the region known as

the entrainment zone. The entrainment zone marks the transition from the PBL to the free atmosphere above. These negative heat fluxes in the entrainment zone are consistent with the observations that downward flux of heat play a large part in heating of the boundary layer as a whole.

UAS have the capability to extend surface measurements in both space and time by rapidly sampling the lower atmosphere, providing new insight to PBL processes. One of the first studies of the diurnal PBL cycle using UAS was performed by Bonin et al. (2012), which focused on the evening transition in the southern great plains of the United States. By collecting numerous consecutive vertical profiles of temperature, humidity, pressure, and winds during the period just before sunset, vertical flux profiles were estimated using a technique suggested by Deardorff et al. (1980):

$$\overline{w'\theta'}(z) = \int_z^{h_a} \left(\frac{\partial \theta}{\partial t} + w \frac{\partial \theta}{\partial z} \right) dz, \tag{6.1}$$

which is the horizontally homogeneous heat balance equation solved for vertical kinematic heat flux, integrated from each level z to height h_a where fluxes go to zero. Equation 6.1 can be further simplified assuming the mean vertical velocity is negligible:

$$\overline{w'\theta'}(z) = \int_z^{h_a} \frac{\partial \theta}{\partial t} dz. \tag{6.2}$$

When accounting for discrete data samples and converting to sensible heat flux, 6.2 becomes:

$$H(z) = c_p \sum_z^{h_a} \rho \frac{\Delta \theta}{\Delta t}(z), \tag{6.3}$$

Where $H(z)$ is the sensible heat flux at level z, c_p is the heat capacity for dry air at constant pressure, and ρ is the density of air evaluated at each level. The same method can be reproduced for latent heat fluxes L by replacing θ with specific humidity q and c_p with latent heat of vaporization, L_v:

$$L(z) = L_v \sum_z^{h_a} \rho \frac{\Delta q}{\Delta t}(z). \tag{6.4}$$

Given ideal conditions of weak background advection, results using this method indicated that as the evening progressed and the boundary layer height decreased, the majority of vertical heat fluxes were confined to increasingly shallow layers just above the surface.

Wildmann et al. (2015) employ the Multi-purpose Airborne Sensor Carrier (MASC), developed by the group of Environmental Physics at the University of Tübingen, which uses fine-wire platinum resistance thermometers and multi-hole probes to directly measure turbulent parameters. Flying constant-altitude profiles 100 meters above the German countryside allowed for application of mixed-layer scaling, which resulted in only being valid for convective temperatures. When compared with a ground-based sonic anemometer and flux measurements, results from these constant-altitude profiles indicated that heat fluxes do not change sign aloft until 2–3 hours after sunrise, and then increase in magnitude as the morning continues. Although the terrain was not entirely horizontally homogeneous in elevation or land use, these results agree with what would be expected from Lapworth (2006).

Even more recently, rotary-wing UAS (rwUAS) are being utilized to collect vertical profiles of atmospheric measurements. One primary advantage rwUAS have over their fixed-wing counterparts is the ability to operate without a launching or landing mechanism, making quasi-unattended operations a possibility. Since the method outlined by Bonin et al. (2012) is not platform-specific, this study seeks to address the capability of rwUAS to obtain vertical flux estimates. This will be done by determining the effectiveness of the algorithm in addition to outlining scenarios in which errors inhibit analysis.

The chapter is structured as follows: in Section 6.2, a description of how the datasets were acquired and how fluxes were estimated is introduced. In Section

6.3, two cases representative of the dataset as a whole are presented. In Section 6.4 conclusions are discussed.

6.2 Data and methods

The CopterSonde rwUAS, as discussed in Section 2.3, is capable of collecting kinematic and thermodynamic measurements similar to traditional radiosondes. Over the course of September 2017 to April 2018, the CopterSonde was flown at the Kessler Atmospheric and Ecological Field Station (KAEFS) in Washington, Oklahoma, during and after sunrise to capture the morning transition period. One advantage this study has compared to previous ones is that CASS is allowed to operate the CopterSonde up to 2500 ft (760 m) AGL beginning 30 min before sunrise at this location via special permissions from the FAA. In general, flight conditions ranged from clear/sunny and calm mornings to cloudy and windy, but were mainly chosen based on lack of clouds or precipitation the night previous. More details about these flights are included in Table 6.1.

Operations typically consisted of consecutive flights once every 15–20 min, and vertical sensible and latent heat fluxes were estimated as in the algorithm outlined by Bonin et al. (2012) in equations (6.3) and (6.4). The height h_a to which each profile is integrated was determined subjectively by identifying the level where values of $\partial\theta/\partial t$ and $\partial q/\partial t$ approach zero, approximately where fluxes no longer influence temperature profiles. This method was supplemented by Doppler wind lidar (DL) measurements when available (see Table 6.1), but still allows room for error due to measurement inconsistencies. These errors will be discussed in more detail in Section 6.3.3.

Table 6.1: Summary of flights conducted at KAEFS with the OU CopterSonde

Date, Civil Twilight	Number of Profiles	Average Δt (min)	CLAMPS	Weather Conditions
21 Sep 2017 1153 UTC	12	21	No	Warm and dry, partly cloudy with moderate southerly winds.
18 Oct 2017 1214 UTC	18	13	No	Sunny, dew in morning, residual LLJ. Strong mixing in transition.
09 Nov 2017 1233 UTC	8	23	No	Mostly sunny, near freezing, and humid. Light winds allowed for sharp inversion which mixed out.
05 Apr 2018 1146 UTC	6	19	Yes	Chilly, dry, breezy, cloudy. Southerly winds. Gradual increase in T and Td.
24 Apr 2018 1121 UTC	12	16	Yes	Calm and clear transitioning to sunny with some cirrus with light winds.

6.3 Results and Discussion

6.3.1 24 April 2018

Around the beginning of civil twilight (1121 UTC) on the morning of April 24, 2018, conditions at KAEFS were clear, humid, and calm with dew on the grass and fog in nearby valleys as evidenced by the Washington Mesonet site located on the property (Figure 6.1). DL measurements indicated that these calm conditions were present aloft as well. This setup allowed for the assumptions used in the Bonin et al. (2012) algorithm: negligible advection and mean vertical velocities. As the morning transition progressed, winds at the surface remained calm (below 3 m s^{-1}) and the skies were clear.

Potential temperature from each flight was interpolated in time at each level and contoured in time-height coordinates (Figure 6.2). Immediately apparent is the strongly stable layer extending from the surface to approximately 200 m AGL, with a considerably less stratified residual layer atop it. The height of this inversion layer appears to grow nearly exponentially with time, eventually becoming well-mixed above 760 m by 15 UTC. This evolution is in excellent agreement with the conceptual model of thermodynamic PBL transitions (Stull, 1988), likely due to the early conditions described above.

Sensible heat fluxes near the surface just after sunrise are negative, even as surface temperatures increase, which supports the hypothesis from previous studies that PBL heating during this time is driven by entrainment (Figure 6.3). As the boundary layer expands throughout the morning, a region of negative sensible heat fluxes follows along the top of the inversion in potential temperature, likely representative of the entrainment zone atop the newly-formed convective boundary layer. Meanwhile, surface sensible heat flux changes sign around 13 UTC, about 2 hrs after sunrise, and increase in magnitude consistently as insolation increases.

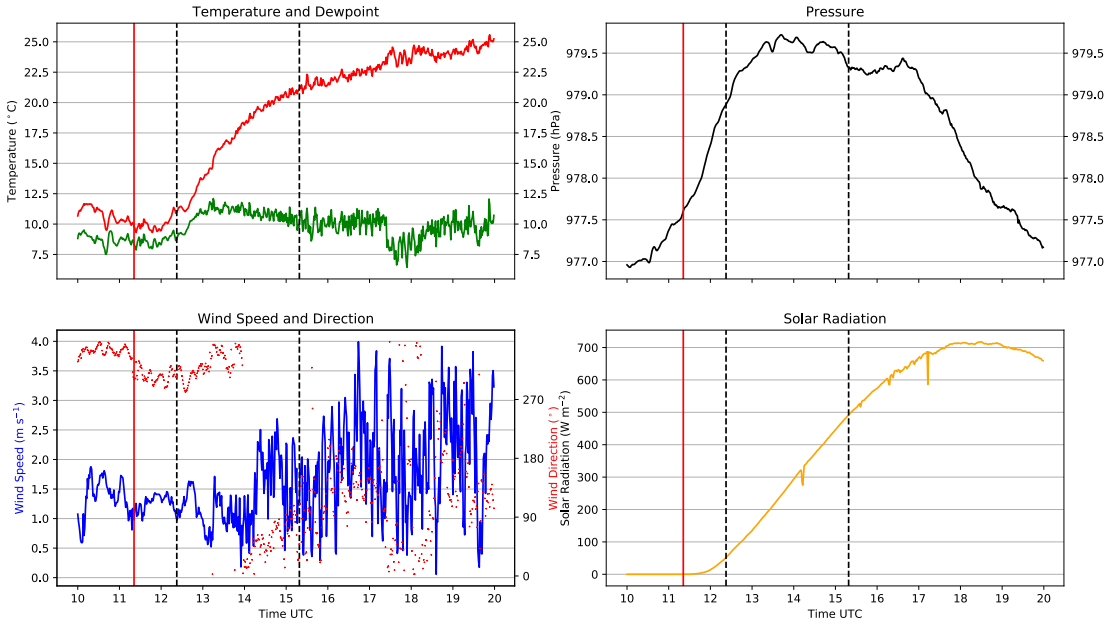

Figure 6.1: 24 April 2018 Meteogram from the Washington Mesonet at KAEFS. The vertical red line represents the beginning of civil twilight, and the vertical black dashed lines are the first and last CopterSonde flights of the day. Top left is Temperature (°C; red) and dewpoint temperature (°C; green); top right is pressure (hPa); bottom left is wind speed (m s^{-1}) and direction (°); and bottom right solar radiation (W m^{-2}).

The relative humidity sensors on the CopterSonde for this case were functional, but not necessarily representative due to their age and number of missions flown. However, their composite mixing ratio results (Figure 6.4) show similar trends of stability and mixing as potential temperature. One notable feature apparent starting at 13 UTC is a large increase in low-level moisture coincident with the time dew had mostly evaporated from the surface. This is reflected in large positive latent heat fluxes at the same time (Figure 6.5). Shortly thereafter, values decrease towards negative as the moisture at the surface decreases, possibly from a larger-scale downdraft from the entrainment zone. Latent fluxes then increase towards

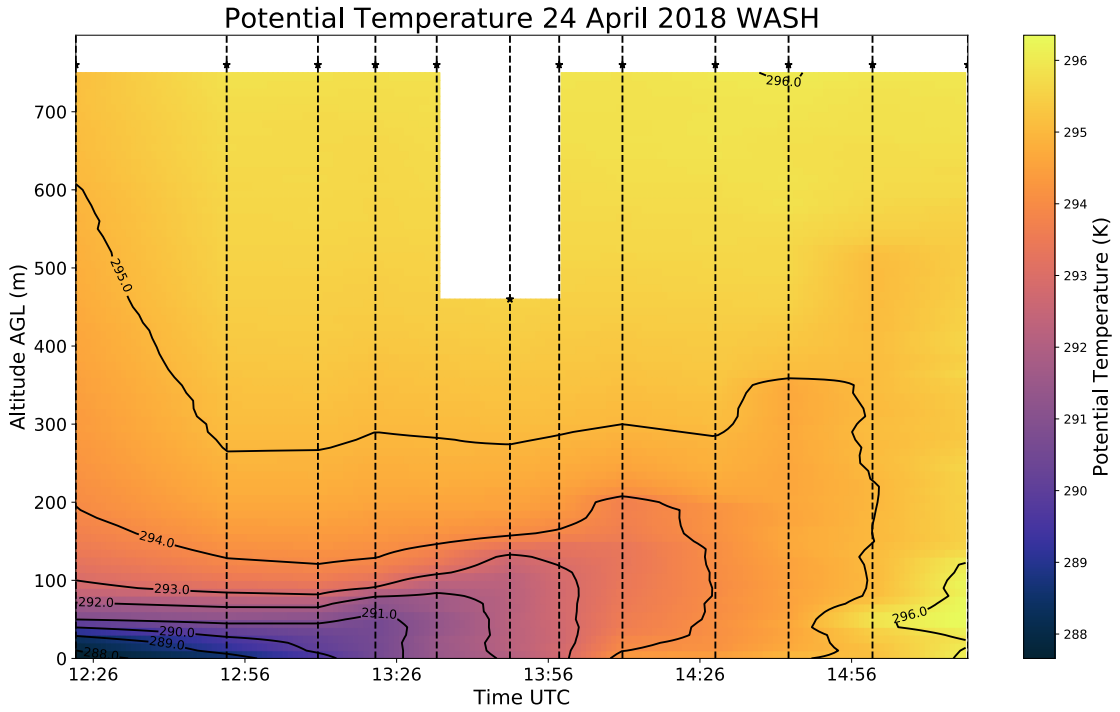

Figure 6.2: 24 April 2018 potential temperature shaded and contoured in time-height coordinates. Several features are present of a classic PBL morning transition, including: stable surface layer directly after sunrise with residual layer atop; inversion height grows exponentially with time; and a well-mixed layer by 15 UTC.

their maximum observed values around 1420 UTC in conjunction with a more rapid expansion of the mixed surface layer.

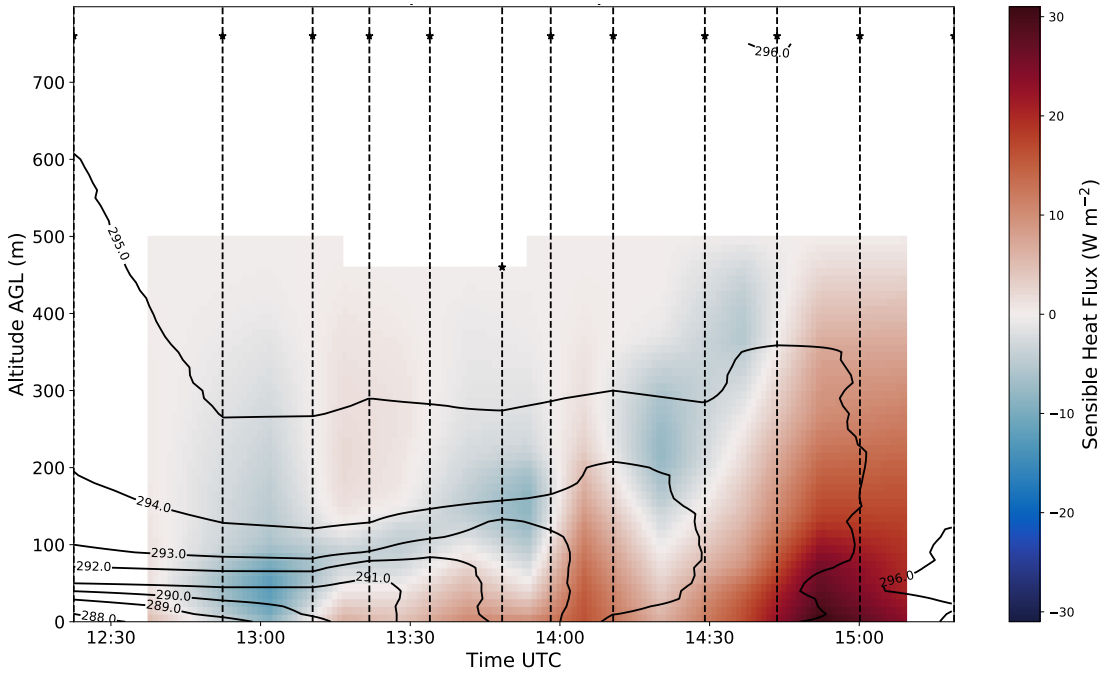

Figure 6.3: 24 April 2018 sensible heat flux (shaded) and potential temperature (contoured). Sensible heat fluxes are weakly negative in early morning. Negative fluxes follow the top of the inversion, representing the entrainment zone. Surface heat fluxes increase in time to strongly positive by 15 UTC.

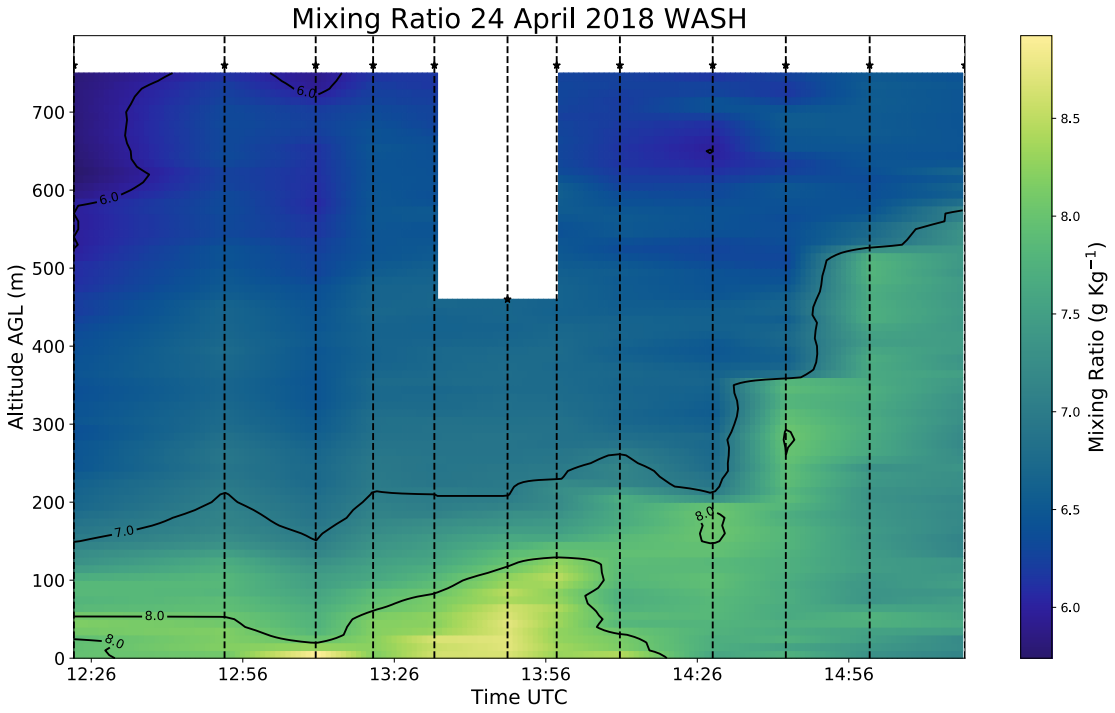

Figure 6.4: 24 April 2018 mixing ratio shaded and contoured. Exponential increase in altitude of the 7.0 g/kg isohume with time as boundary layer expands. Strong surface moisture increase starting 13 UTC and subsequent decrease an hour later as the moisture is mixed out.

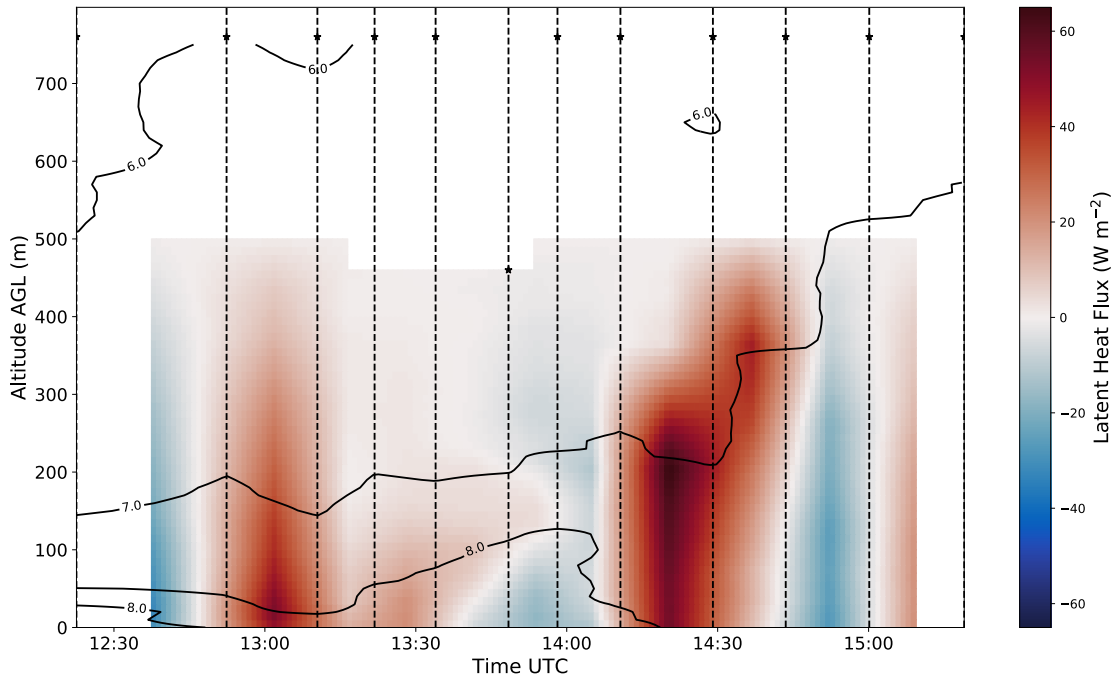

Figure 6.5: 24 April 2018 latent heat flux (shaded) and specific humidity (contoured). Strong fluxes at 13 UTC as dew and fog in the region evaporated, and subsequent decrease at 14 UTC as moisture from aloft is transported downwards. At 1430 UTC, another positive flux profile with a maximum at the top of the entrainment zone, which turns negative again by 15 UTC with further mixing.

6.3.2 18 October 2017

The morning of 18 October 2017 was clear, humid, and calm, not unlike the morning of April 24 described previously. Civil twilight began at 1214 UTC. However, one key difference was the presence of a residual low level jet with winds of 20–25 m s^{-1} at 400–500 m AGL. While surface winds were initially calm at the surface (around 2 m s^{-1}) after sunrise, momentum rapidly mixed downward starting at 14 UTC when surface winds nearly quadrupled in just an hour (Figure 6.6). Agreement between the CopterSonde and Washington Mesonet observations were generally good for the duration of the observed timeframe (Figure 6.7).

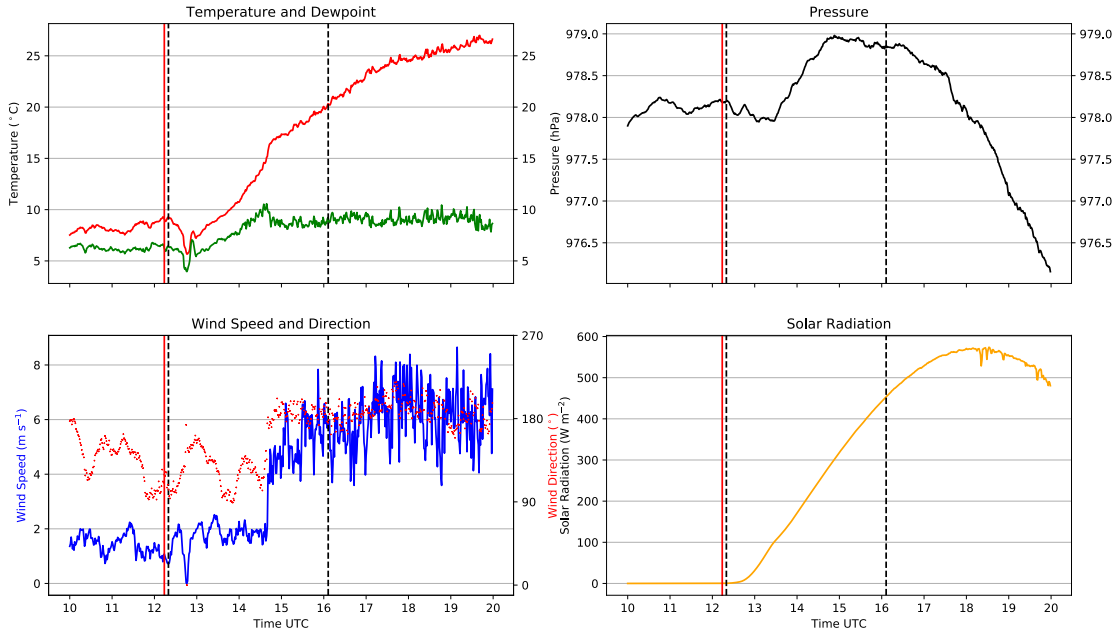

Figure 6.6: 18 October 2017 time series graph of data from the Washington Mesonet site. Red and black vertical lines denote same as in Figure 6.1. Similar to the case from 24 April, the morning was humid after sunrise and dewpoints stagnated after 14 UTC with mixing. There is a discontinuity in wind speed and direction at 14 UTC as momentum is rapidly transferred downwards.

The transition in potential temperature (Figure 6.8) is also similar to the classical model, with a stably-stratified layer persisting until about 1430 UTC when

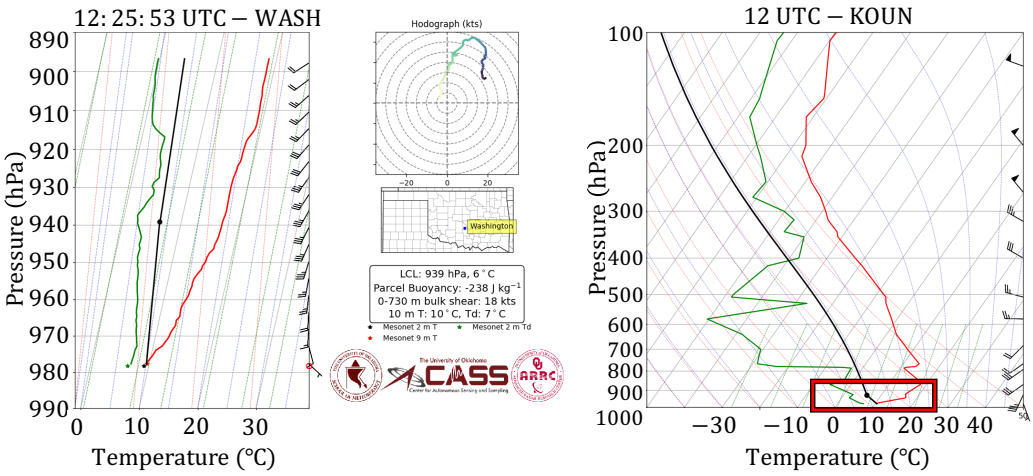

Figure 6.7: First CopterSonde profile from 12:26 UTC on 18 October 2017 (left) in comparison to the 12 UTC sounding launched from KOUN just 30 km away (right). The black, red, and green stars at the base of the CopterSonde profile represent 2 m and 9 m temperature and 2 m dewpoint temperature measurements, respectively, from the Washington Mesonet tower closest to the profile time, which are in excellent agreement with CopterSonde temperature and dewpoint. The red box on the KOUN sounding represents the approximate same range of pressures as the CopterSonde flight, which indicates a similar strength in thermal inversion

the boundary layer seems to expand rapidly. A mixed layer from the surface to 300 m persists for the remainder of the time period, with a considerably stable region directly above.

The trends in estimated vertical sensible heat fluxes are not necessarily as straightforward (Figure 6.9). Sensible heat fluxes begin weakly negative and quickly transition to positive within half an hour, around 13 UTC. Afterwards, the column transitions back and forth from positive to negative several times until 1430 UTC. Because of the strong winds present aloft, it is possible this is a result

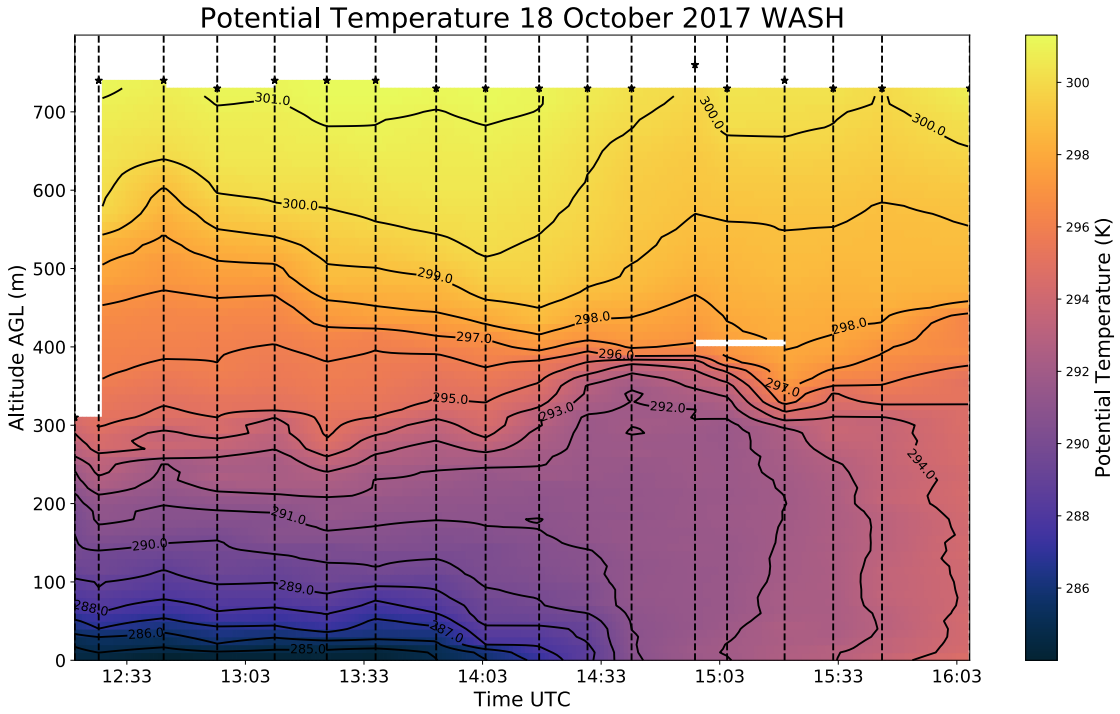

Figure 6.8: 18 October 2017 potential temperature as measured by the 18 rwUAS profiles shaded and contoured. Strongly stable surface layer gives way to well-mixed PBL starting around 1430 UTC. Appreciably stable zone exists at 400 m AGL atop mixed layer after the rapid transport downward of momentum due to vertical mixing.

of observing large-scale rising and sinking motion as mechanical turbulence production is spread throughout the PBL. This hypothesis is supported by the abrupt change from 2 m s^{-1} to 5 m s^{-1} in wind speeds at 14 UTC (Figure 6.6) signifying rapid downward transport of momentum in conjunction with the strongly negative sensible heat fluxes at this time. Afterwards, the transition proceeds similar to the previous case, with positive sensible heat fluxes from the surface to the top of the inversion, where fluxes change sign due to downward entrainment.

Mixing ratio (Figure 6.10) also depicts a similar PBL transition, notably with strong stratification in the early morning at both the surface to 200 m and above 500 m AGL. These regions converge atop a surge in moisture around 1430 UTC,

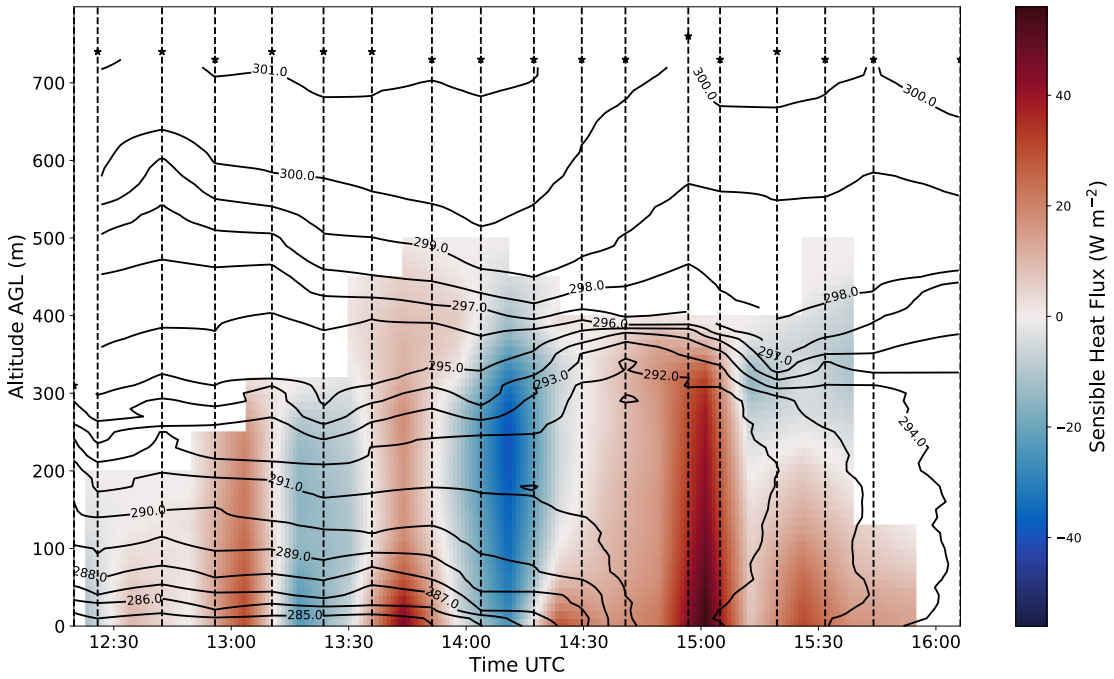

Figure 6.9: 18 October 2017 sensible heat flux (shaded) and potential temperature (contoured) as measured from the 18 rwUAS profiles. Alternating positive and negative heat fluxes from 1300 – 1430 UTC possibly due to alternating updrafts and downdrafts in vertical mixing. Strong negative fluxes at 14 UTC coincident with downward transport of momentum concentrated at top of the inversion layer. Positive surface fluxes at 15 UTC and subsequent well-mixed layer, with negative fluxes atop inversion implying entrainment zone.

after which a well-mixed layer extends from the surface to 300 m AGL. This pulse of moisture is almost identical to the one observed in the previous case around the same time after sunrise.

Latent heat fluxes on this day as calculated from the potential temperature observations (Figure 6.11) tended to oscillate between positive and negative until 14 UTC, when these fluxes increased to strongly positive in conjunction with the rapid moistening of the layer and mixing down of momentum. The sign of latent heat fluxes tended to oppose that of sensible heat fluxes for the first few hours

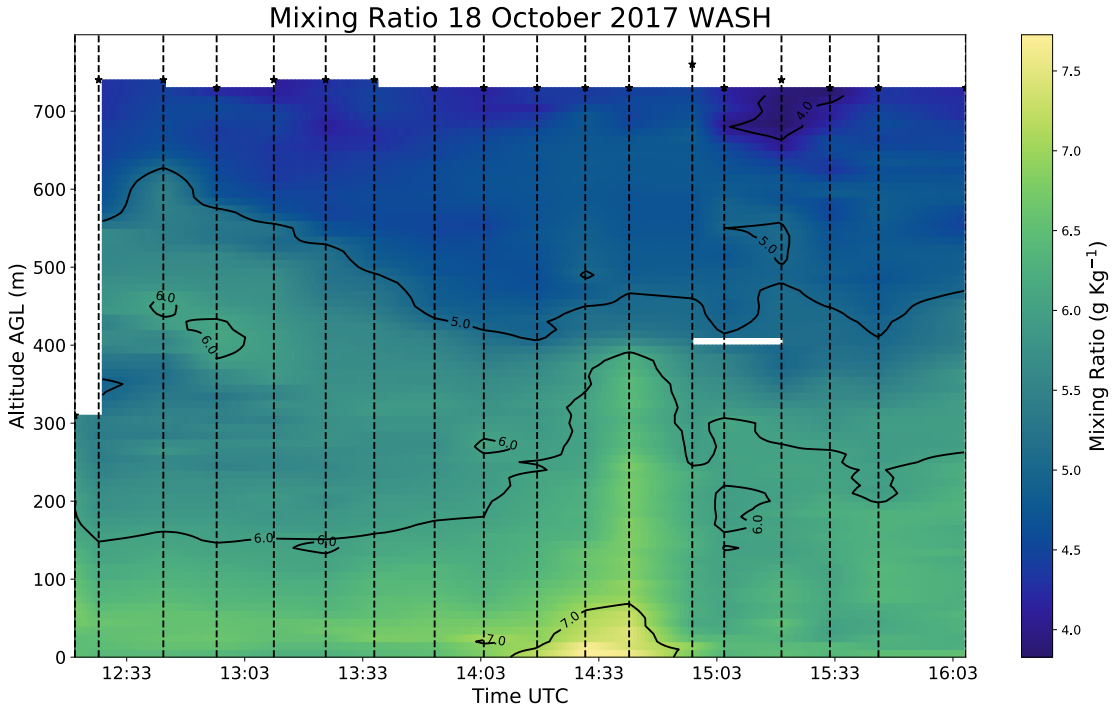

Figure 6.10: 18 October 2017 mixing ratio measured by the rwUAS profiles contoured and shaded. Strong stratification from the surface to 200 m AGL and another zone of stratification from 500–700 m. These regions ascend and descend, respectively, until they converge around 1430 UTC with coincident pulse in surface moisture. There is a well-mixed layer afterwards with stratification above.

following sunrise (Figure 6.12). This opposition was most significant at 14 UTC where sensible heat fluxes are strongly *negative* in accordance with the downward momentum flux, whereas latent heat fluxes are strongly *positive*, close to around the time dew and fog evaporated at the surface. Both of these change sign again shorty thereafter as the PBL expanded rapidly.

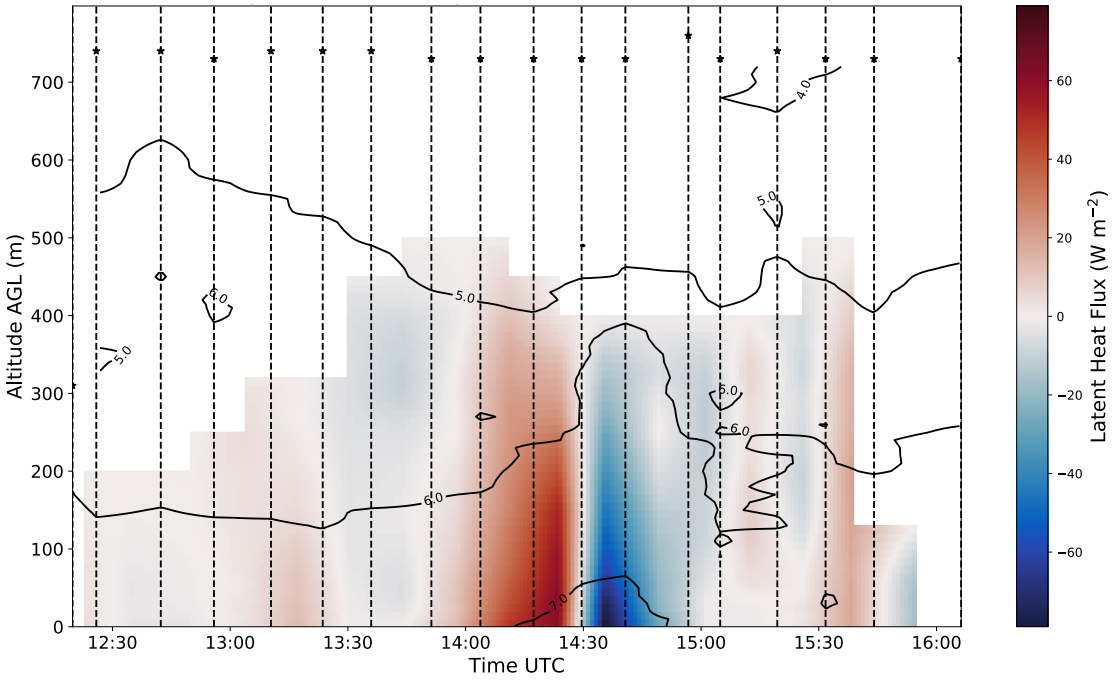

Figure 6.11: 18 October 2017 latent heat flux (shaded) and specific humidity (contoured) measured from the rwUAS profiles. Weak flux magnitudes after sunrise until 14 UTC coincident with moisture pulse, and subsequent negative fluxes as moisture is mixed down with vertical mixing.

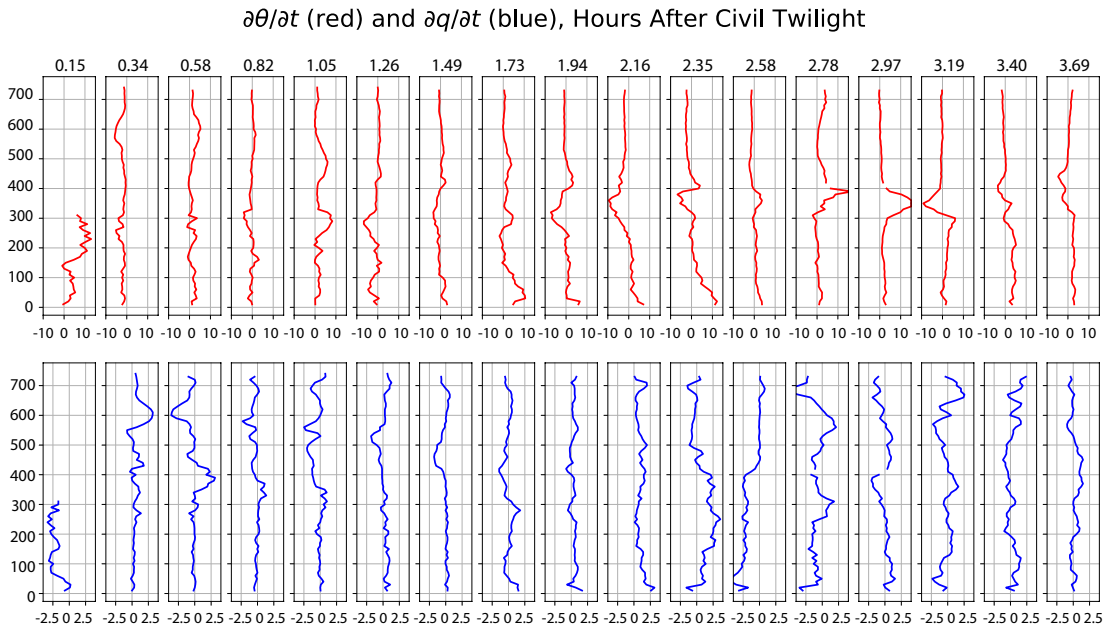

Figure 6.12: 18 October 2017 sensible (red) and latent heat flux (blue) vertical profiles for each analysis timestep. Often times, these two mechanisms counteract one another. This is especially apparent in the 10th panel (2.16 hrs after civil twilight), which is coincident with the downward transport in sensible heat flux and momentum but surge in moisture from the surface. These both change signs again by the 12th panel (2.58 hrs), likely when vertical mixing has increased in depth.

6.3.3 Discussion

Given the results from 24 April that is representative of other cases not discussed, it appears that the method of estimating fluxes from Bonin et al. (2012) is reasonable and applicable for rwUAS when the underlying assumptions are in place. Sensible heat fluxes from this day closely agree with observations and simulations in the literature, and latent heat fluxes appear reasonable even with their associated caveats.

Evaluation of 18 October is less certain, namely because the presence of strong flow aloft is inconsistent from the algorithm's assumption of homogeneity and zero wind shear. Although the resulting fluxes do not follow the trend of a typical morning PBL evolution, it is possible to infer physical mechanisms associated with specific features. There appears to have been a large downdraft around 14 UTC which acted to transport momentum and sensible heat downwards from the top of the inversion layer, which was opposed by an upward transport of latent heat. By 1430 UTC, the opposite end of this vertical circulation was observed with a reversal of the sensible and latent heat fluxes.

While these explanations seem to adequately describe the observations, it is also within reason that these flux estimates are prone to errors. The method of calculation is highly sensitive to errors in measurements, and visual inspection showed an appreciable amount of noise in the rate of change profiles (Figure 6.12) with subjectively-chosen levels of assumed zero flux. Data in this study were not smoothed after post-processing the raw observations, and doing so could potentially lead to improved results. Future plans for evaluating this method will compare similar days involving low level jets by also incorporating surface flux station data as validation.

6.4 Chapter Conclusions

A novel method of estimating vertical sensible and latent heat fluxes using rwUAS was performed over the period of September 2017 to April 2018 in central Oklahoma using the CopterSonde rwUAS developed by CASS. This method, first suggested by Deardorff et al. (1980) and implemented by Bonin et al. (2012) using a fixed-wing UAS, involves the rate of change in potential temperature and specific humidity at each level between consecutive profiles (equations (6.3) and (6.4)). When the PBL represented negligible horizontal advection and weak mean vertical winds, this method produced results that align well with theory: entrainment was the primary driver of PBL heating for several hours after sunrise, and an explicit entrainment zone was evident. Observed latent heat fluxes reflected moisture from surface evaporation transported vertically through the PBL.

Even during conditions when the method's assumptions were not necessarily met, this method provides insight to mixed-layer processes occurring during the morning transition. Large increases in momentum were collocated with increases in sensible heat flux, and decreases in latent heat flux. More data will need to be collected under similar conditions to determine if these features are physical or resultant from inconsistencies between measurements and/or invalid assumptions.

Overall, this method appears to have merit as a tool to diagnose PBL processes across local and nonlocal scales. By incorporating observations from other ground-based stations (eddy covariance station, DL, etc.), we may be able to gain further insights into how turbulence drives boundary layer growth and decay.

Chapter 7

Conclusions and Remarks

Given the limitations of present observational networks, researchers are experimenting with UAS as a method to bridge the data void in the lower atmosphere. Development of unmanned aircraft for this application has taken advantage of technological advancements in manned research aircraft, so several groups have focused efforts on fixed-wing UASs. These systems can cover large horizontal distances with several hours of flight duration while utilizing fast-response sensors and have already shown great promise for applications including turbulence characterization, wind energy forecasting, convective storm environmental sampling, and trace gas plume identification. Even more recently, rotary-wing UAS are being realized as a viable complement to fwUAS, namely for their takeoff and landing procedures requiring little human intervention. Multicopters typically have shorter maximum flight durations than fwUAS, but their simplified operations have the advantage of being able to perform missions rapidly in succession or even potentially operate unattended.

Realizing the potential for UASs to reshape the state of atmospheric sciences, the NSF, NOAA, and OU VPR have supported CASS at OU to establish a foundation for conducting research in this field. By capitalizing on the strengths in atmospheric physics, engineering, and aviation at OU required for this mission, CASS has made meaningful strides in the development of UASs for atmospheric

research. This study has detailed the multi-faceted approach to developing rwUASs for PBL profiling along with results from several applications.

7.1 Summary

With the objective to design and implement a rotay-wing UAS for vertical thermodynamic and kinematic profiling, efforts were focused into three main steps: 1. select a sensor package that offers high quality measurements out of the box and calibrate them to determine their reliabilities; 2. integrate these sensors with a rwUAS, characterize their new responses, and develop a method of estimating horizontal winds; and 3. evaluate the quality of measurements by collecting real-world observations with scientific objectives. The results from these objectives are as follows:

1. The iMet-XF sensors were advertised to be within NOAA standards, which was verified when calibrated in an Oklahoma Mesonet environmentally controlled chamber and aspirated chamber on the NWC Mesonet tower. These sensors were preferred over the Windsond package due to their onboard synchronization and unified data stream.

2. Experiments identified that the iMet thermistors suffered from self-heating when not properly aspirated, and that it is possible to obtain reliable temperature measurements when using the propeller wash as aspiration. A rwUAS introduces several sources of error, such as heating from the motors in addition to compressional and frictional heating from the propeller tips. Placement of temperature sensors 10 cm underneath the propeller and one quarter its length from the tip can mitigate these biases. Furthermore, a statistical model for estimating wind speeds using Euler angles derived from the

rwUAS's autopilot was developed and produced measurements close to the NOAA specifications.

3. The CopterSonde was tested during the EPIC field campaign in May of 2017, and proved capable of providing reliable measurements in pre-convective environments which were relayed to forecasters at the NWS. This campaign greatly streamlined operations in the field by improving ground station technology, communication between team members, and visualization of data. Additionally, the CopterSonde was used for collecting measurements detailing the structure of the atmosphere during morning PBL transitions at KAEFS. These measurements validated well against the nearby Mesonet tower and KOUN soundings, and usually agreed with the conceptual model of the diurnal PBL cycle. A method for estimating vertical heat flux profiles was also evaluated using these collected data, and results are consistent with those in the literature provided conditions of homogeneity and weak winds are met. Results from days not meeting these criteria still provide merit to the algorithm, which shows promise for future studies using rwUAS to measure PBL processes.

Through a systematic approach to the challenge of unifying the disciplines of engineering, physics, and meteorology, this study has demonstrated that rwUASs can be successfully optimized to bridge the gap in lower atmospheric observations identified by the National Research Council (2009). With the results from this study, future implementation of UAS technology shows potential to reshape the landscape of atmospheric sensing and sampling.

7.2 Future Work

The CopterSonde's development has been insightful to the optimization of UAS design for various applications. While its eight powerful motors enable it to withstand severe thunderstorm force winds, this design compromises flight endurance due to its weight and size. In some cases, it may be advantageous to prioritize endurance and mobility over maximum power output, for example when there are fewer restrictions on maximum flight altitude. Realizing this, CASS has also already designed and built a new generation of CopterSonde, termed the "CopterSonde 2.0". This rwUAS is significantly more compact and lightweight, is equipped with real-time differential GPS, and new advancements in software development allow it to stream data to a webpage in real-time for remote viewing. One of the models also incorporates a ducted fan as a method to aspirate sensors more consistently than using propeller wash, and has shown promising results.

The CopterSonde 2.0 was developed in preparation for CASS participation in the Innovative Strategies for Observations in the Arctic Atmospheric Boundary Layer (ISOBAR) field campaign. This project took place in February of 2018 on the island of Hailuoto, Finland, located at 65° North latitude, and investigated the winter stable boundary layer above sea ice using a fleet of UAVs. ISOBAR participants included the University of Bergen (Norway), the Finnish Meteorological Institute, the University of Tübingen (Germany), the University of Applied Science Ostwestfalen-Lippe (Germany), and OU, the only group from outside of Europe. These groups represent some of the world leaders in the field of UAS in atmospheric sciences, as they have developed several advanced custom-built platforms of their own for past field campaigns. Instrumentation for ISOBAR also included two sodars, a Doppler lidar, a 10 m tower with 3 eddy covariance stations, and a 2 m tower with an eddy covariance station. In addition to the climate of interest for meteorological purposes, the flight regulations in Finland were also

advantageous to operations. Flights were allowed up to 6500 ft (1980 m) AGL, and were permissible at night and beyond visual line of sight, none of which are the case in the United States for typical small UAS applications. These rules allowed flights through cloud decks and enabled continuous monitoring of the onset of stable boundary layers overnight, which was crucial to the scientific objectives. During intensive operational periods (IOPs), CASS performed continuous vertical profiles with the CopterSonde 2.0 launching from the sea ice in proximity to the instrumented towers. IOPs typically lasted the whole night, so teams would adhere to schedules of a few hours flying followed by a few hours of rest. In between these IOPs, the CASS team experimented with two other fixed-wing aircraft designed specifically for photogrammetry and carbon dioxide measurements, respectively. Overall, the campaign was largely successful. Numerous international groups combined expertise and collected valuable data in extremely inhospitable conditions. The experiences by the CASS team significantly improved operational capabilities with the new designs of platforms performing beyond expectations. Successful operations in flight conditions not experienced or allowed in the United States should assist in the confidence of the regulatory agencies and ease the transition of increased UAV activity in the national airspace. The data collected are currently undergoing quality control by the participating members, and their future analysis is highly anticipated.

Development of even newer generations of CopterSonde is also ongoing. A new experimental version combining the strengths of the two variations on the CopterSonde 2.0 is on pace to be completed for a field campaign in July 2018. This campaign includes members of the International Society for Atmospheric Research using Remotely Piloted Aircraft (ISARRA) who will be combining efforts to sample the atmosphere in the San Luis Valley in Southern Colorado. This region is at an elevation of about 7500 ft above sea level and surrounded by mountains

rising almost a mile above the valley floor to the North, East, and West. This complex terrain provides a great opportunity to examine drainage flows, boundary layer transitions, convection initiation, trace gas, and aerosol concentrations above farmland, grassy plains, rivers, and sand dunes. This large collective effort should prove to be an interesting case study that will continue to demonstrate the utility of UAS in atmospheric sciences.

Presently, CASS's most significant long-term project is known as the 3D Mesonet. This concept begins with the utility of mesoscale surface observational networks like the Oklahoma Mesonet, and addresses their limitations in vertical extent by integrating fully autonomous, unattended vertically profiling rwUAS at each site. Success in this implementation would redefine the standard for observational networks, providing an entire volume of thermodynamic and kinematic data across the entire state of Oklahoma with mesoscale resolution. Access to these observations will require innovations in data visualization techniques, and can provide forecasters with new perspectives of weather features like fronts and drylines. The potential benefits of the 3D Mesonet are immense across several disciplines, but the infrastructure required for its implementation is almost equally as large. Not only do the systems have to provide reliable measurements, it must be hardened enough to do it regularly and consistently for long periods of time in varying conditions. An unattended system would require a means to recharge batteries quickly, likely facilitating wireless charging technology inside of the automated shelter for the UAV. The link from aircraft to ground station must be robust and have failsafes to prevent loss of communication. This link must also maintain a level of encryption to prevent unauthorized control of the UAV. The ground stations will require a streamlined interface and upload protocol for uniform data quality across sites at a central data server, which must also be accessible to the public in near-real time after quality control and post processing. To maintain a safe airspace

while operating unattended, safety features like a detect and avoid radar will scan the surrounding airspace for obstacles and relay information to the UAV to avoid collisions. The systems will also be outfitted with a radio transponder to alert other manned aircraft of its position at all times. These measures are just some of those required to fill the role of human operators during normal operations, and as such will take several years worth of research and development. Fortunately, the lessons learned and experiences gained through the development of the original CopterSonde in this study have already laid significant foundations for turning this concept into a reality.

Bibliography

Agustí-Panareda, A., A. Beljaars, C. Cardinali, I. Genkova, and C. Thorncroft, 2010: Impacts of assimilating AMMA soundings on ECMWF analyses and forecasts. *Weather and Forecasting*, **25 (4)**, 1142–1160, doi:10.1175/2010WAF2222370.1.

Angevine, W. M., H. K. Baltink, and F. C. Bosveld, 2001: Observations of the morning transition of the convective boundary layer. *Boundary-Layer Meteorology*, **101**, 209–227.

Ashley, W. S., S. Strader, D. C. Dziubla, and A. Haberlie, 2015: Driving blind: Weather-related vision hazards and fatal motor vehicle crashes. *Bulletin of the American Meteorological Society*, **96 (5)**, 755–778, doi:10.1175/BAMS-D-14-00026.1.

Bailey, S. C. C., B. M. Witte, C. Schlagenhauf, B. R. Greene, and P. B. Chilson, 2017: Measurement of high Reynolds number turbulence in the atmospheric boundary layer using unmanned aerial vehicles. International Symposium on Turbulence and Shear Flow Phenomena, Vol. 10.

Banta, R. M., and Coauthors, 2015: 3d volumetric analysis of wind turbine wake properties in the atmosphere using high-resolution Doppler lidar. *J. Atmos. Ocean. Tech.*, **32 (5)**, 904–914, doi:10.1175/JTECH-D-14-00078.1.

Båserud, L., J. Reuder, M. O. Jonassen, S. T. Kral, M. B. Paskyabi, and M. Lothon, 2016: Proof of concept for turbulence measurements with the RPAS SUMO during the BLLAST campaign. *Atmos. Meas. Tech.*, **9 (10)**, 4901, doi:10.5194/amt-9-4901-2016.

Benjamin, S. G., B. D. Jamison, W. R. Moninger, S. R. Sahm, B. E. Schwartz, and T. W. Schlatter, 2010: Relative short-range forecast impact from aircraft, profiler, radiosonde, VAD, GPS-PW, METAR, and mesonet observations via the RUC hourly assimilation cycle. *Monthly Weather Review*, **138 (4)**, 1319–1343, doi:10.1175/2009MWR3097.1.

Blumberg, W. G., T. J. Wagner, D. D. Turner, and J. J. Correia, 2017: Quantifying the accuracy and uncertainty of diurnal thermodynamic profiles and

convection indices derived from the atmospheric emitted radiance interferometer. *Journal of Applied Meteorology and Climatology*, **56 (10)**, 2747–2766, doi:10.1175/JAMC-D-17-0036.1.

Bonin, T., P. Chilson, B. Zielke, and E. Fedorovich, 2012: Observations of the early evening boundary-layer transition using a small unmanned aerial system. *Boundary-Layer Meteorology*, **146 (1)**, 119–132, doi:10.1007/s10546-012-9760-3, URL http://dx.doi.org/10.1007/s10546-012-9760-3.

Bonin, T., P. Chilson, B. Zielke, P. Klein, and J. Leeman, 2013: Comparison and application of wind retrieval algorithms for small unmanned aerial systems. *Geoscientific Instrumentation, Methods and Data Systems*, **2 (2)**, 177–187.

Bonin, T. A., W. G. Blumberg, P. M. Klein, and P. B. Chilson, 2015: Thermodynamic and turbulence characteristics of the southern great plains nocturnal boundary layer under differing turbulent regimes. *Bound.-Lay. Meteorol.*, **157 (3)**, 401–420, doi:10.1007/s10546-015-0072-2.

Bonner, W. D., 1968: Climatology of the low level jet. *Monthly Weather Review*, **96 (12)**, 833–850, doi:10.1175/1520-0493(1968)096⟨0833:COTLLJ⟩2.0.CO;2.

Brock, F. V., K. C. Crawford, R. L. Elliott, G. W. Cuperus, S. J. Stadler, H. L. Johnson, and M. D. Eilts, 1995: The Oklahoma Mesonet: a technical overview. *J. Atmos. Ocean. Tech.*, **12 (1)**, 5–19, doi:10.1175/1520-0426(1995)012⟨0005:TOMATO⟩2.0.CO;2.

Brosy, C., K. Krampf, M. Zeeman, B. Wolf, W. Junkermann, K. Schäfer, S. Emeis, and H. Kunstmann, 2017: Simultaneous multicopter-based air sampling and sensing of meteorological variables. *Atmos. Meas. Tech.*, **10 (8)**, 2773–2784, doi:10.5194/amt-10-2773-2017.

Charba, J., 1974: Application of gravity current model to analysis of squall-line gust front. *Mon. Weather Rev.*, **102 (2)**, 140–156, doi:10.1175/1520-0493(1974)102⟨0140:AOGCMT⟩2.0.CO;2.

Chilson, P., A. Gleason, B. Zielke, F. Nai, M. Yeary, P. Klein, and W. Shalamunec, 2009: SMARTSonde: A small uas platform to support radar research. *AMS 34th Conf. Radar Meteor.*, Boston, MA. Am. Meteorol. Soc.

Chilson, P. B., J. Jacob, S. Smith, and A. L. Houston, 2016: CLOUD-MAP: Advancing meteorology and atmospheric physics through unmanned aerial systems. *96th Annual Meeting*, New Orleans, LA, American Meteorological Society, 4.1, https://ams.confex.com/ams/96Annual/webprogram/Paper290287.html.

Cohen, A. E., M. C. Coniglio, S. F. Corfidi, and S. J. Corfidi, 2007: Discrimination of mesoscale convective system environments using sounding observations. *Weather and Forecasting*, **22 (5)**, 1045–1062, doi:10.1175/WAF1040.1.

de Boer, G., and Coauthors, 2016: The Pilatus unmanned aircraft system for lower atmospheric research. *Atmos. Meas. Tech.*, **9 (4)**, 1845–1857, doi:10.5194/amt-9-1845-2016.

Deardorff, J. W., G. E. Willis, and B. H. Stockton, 1980: Laboratory studies of the entrainment zone of a convectively mixed layer. *Journal of Fluid Mechanics*, **100**, 41–64.

Faccani, C., and Coauthors, 2009: The impacts of AMMA radiosonde data on the french global assimilation and forecast system. *Weather and Forecasting*, **24 (5)**, 1268–1286, doi:10.1175/2009WAF2222237.1.

Fedorovich, E., and Coauthors, 2004: Entrainment into sheared convective boundary layers as predicted by different large eddy simulation codes. *16th Symp. on Boundary Layers and Turbulence*, American Meteorological Society, 4.7.

Garratt, J., 1992: *The Atmospheric Boundary Layer*. 1st ed., Cambridge University Press, 316 pp.

Geerts, B., and Coauthors, 2017: The 2015 Plains Elevated Convection at Night field project. *Bulletin of the American Meteorological Society*, **98 (4)**, 767–786, doi:10.1175/BAMS-D-15-00257.1.

Gensini, V. A., T. L. Mote, and H. E. Brooks, 2014: Severe-thunderstorm reanalysis environments and collocated radiosonde observations. *Journal of Applied Meteorology and Climatology*, **53 (3)**, 742–751, doi:10.1175/JAMC-D-13-0263.1.

Gioli, B., F. Miglietta, F. P. Vaccari, A. Zaldei, and B. De Martino, 2006: The sky arrow ERA, an innovative airborne platform to monitor mass, momentum and energy exchange of ecosystems. *Ann. Geophys.-Italy*, **49 (1)**, URL http://www.ann-geophys.net/49/109/2006/.

Greene, B. R., A. R. Segales, S. Waugh, S. Duthoit, and P. B. Chilson, 2018: Considerations for temperature sensor placement on rotary-wing unmanned aircraft systems. *Atmospheric Measurement Techniques Discussions*, doi:10.5194/amt-2018-65.

Grund, C. J., R. M. Banta, J. L. George, J. N. Howell, M. J. Post, R. A. Richter, and A. M. Weickmann, 2001: High-resolution Doppler lidar for boundary layer and cloud research. *J. Atmos. Ocean. Tech.*, **18 (3)**, 376–393, doi:10.1175/1520-0426(2001)018⟨0376:HRDLFB⟩2.0.CO;2.

Hardesty, R. M., and R. M. Hoff, 2012: Thermodynamic profiling technologies workshop report to the national science foundation and the national weather service. Tech. Rep. NCAR/TN-488+STR, National Center for Atmospheric Research. doi:10.5065/D6SQ8XCF.

Houston, A. L., B. Argrow, J. Elston, J. Lahowetz, E. W. Frew, and P. C. Kennedy, 2012: The Collaborative Colorado–Nebraska Unmanned Aircraft System Experiment. *Bulletin of the American Meteorological Society*, **93 (1)**, 39–54, doi:10.1175/2011BAMS3073.1.

Hubbard, K., X. Lin, C. Baker, and B. Sun, 2004: Air temperature comparison between the MMTS and the USCRN temperature systems. *J. Atmos. Ocean. Tech.*, **21 (10)**, 1590–1597, doi:10.1175/1520-0426(2004)021⟨1590:ATCBTM⟩2.0.CO.

Jacob, J. D., P. B. Chilson, A. L. Houston, and S. W. Smith, 2018: Considerations for atmospheric measurements with small unmanned aircraft systems. *Atmosphere*, **9 (7)**, doi:10.3390/atmos9070252, URL http://www.mdpi.com/2073-4433/9/7/252.

Koch, S. E., R. Ware, H. Jiang, and Y. Xie, 2016: Rapid mesoscale environmental changes accompanying genesis of an unusual tornado. *Weather and Forecasting*, **31 (3)**, 763–786, doi:10.1175/WAF-D-15-0105.1.

Konrad, T. G., M. L. Hill, J. H. Meyer, and J. R. Rowland, 1970: A small, radio-controlled aircraft as a platform for meteorological sensors. *Applied Physics Lab Technical Digest*, **10**, 11–19.

Kosiba, K., J. Wurman, Y. Richardson, P. Markowski, P. Robinson, and J. Marquis, 2013: Genesis of the Goshen County, Wyoming, tornado on 5 june 2009 during VORTEX2. *Monthly Weather Review*, **141 (4)**, 1157–1181, doi:10.1175/MWR-D-12-00056.1.

Lackmann, G., 2011: *Midlatitude Synoptic Meteorology: Dynamics, Analysis, and Forecasting*. American Meteorological Society.

Lanzante, J. R., S. A. Klein, and D. J. Seidel, 2003: Temporal homogenization of monthly radiosonde temperature data. part i: Methodology. *Journal of Climate*, **16 (2)**, 224–240, doi:10.1175/1520-0442(2003)016⟨0224:THOMRT⟩2.0.CO;2.

Lapworth, A., 2006: The morning transition of the nocturnal boundary layer. *Boundary-Layer Meteorology*, **119 (3)**, 501–526, doi:10.1007/s10546-005-9046-0, URL http://dx.doi.org/10.1007/s10546-005-9046-0.

Lothon, M., and Coauthors, 2014: The BLLAST field experiment: boundary-layer late afternoon and sunset turbulence. *Atmos. Chem. Phys.*, **14 (20)**, 10 931–10 960, doi:10.5194/acp-14-10931-2014.

Luers, J. K., and R. E. Eskridge, 1998: Use of radiosonde temperature data in climate studies. *Journal of Climate*, **11 (5)**, 1002–1019, doi:10.1175/1520-0442(1998)011⟨1002:UORTDI⟩2.0.CO;2.

Lundquist, J. K., and Coauthors, 2017: Assessing state-of-the-art capabilities for probing the atmospheric boundary layer: the XPIA field campaign. *B. Am. Meteorol. Soc.*, **98 (2)**, 289–314, doi:10.1175/BAMS-D-15-00151.1.

Markowski, P. M., 2016: An idealized numerical simulation investigation of the effects of surface drag on the development of near-surface vertical vorticity in supercell thunderstorms. *Journal of the Atmospheric Sciences*, **73 (11)**, 4349–4385, doi:10.1175/JAS-D-16-0150.1.

Markowski, P. M., and G. H. Bryan, 2016: Les of laminar flow in the PBL: A potential problem for convective storm simulations. *Monthly Weather Review*, **144 (5)**, 1841–1850, doi:10.1175/MWR-D-15-0439.1.

McPherson, R. A., and Coauthors, 2007: Statewide monitoring of the mesoscale environment: A technical update on the Oklahoma Mesonet. *J. Atmos. Ocean. Tech.*, **24 (3)**, 301–321, doi:10.1175/JTECH1976.1.

National Research Council, 2007: *Earth Science and Applications from Space: National Imperatives for the Next Decade and Beyond*. National Academies Press, 456 pp.

National Research Council, 2009: *Observing weather and climate from the ground up: A nationwide network of networks*. National Academies Press.

Neumann, P. P., and M. Bartholmai, 2015: Real-time wind estimation on a micro unmanned aerial vehicle using its inertial measurement unit. *Sensor Actuat. A-Phys.*, **235**, 300–310, doi:10.1016/j.sna.2015.09.036.

Nowotarski, C. J., P. M. Markowski, and Y. P. Richardson, 2011: The characteristics of numerically simulated supercell storms situated over statically stable boundary layers. *Monthly Weather Review*, **139 (10)**, 3139–3162, doi:10.1175/MWR-D-10-05087.1.

Palomaki, R. T., N. T. Rose, M. van den Bossche, T. J. Sherman, and S. F. De Wekker, 2017: Wind estimation in the lower atmosphere using multirotor aircraft. *J. Atmos. Ocean. Tech.*, **34 (5)**, 1183–1191, doi:10.1175/JTECH-D-16-0177.1.

Parker, M. D., 2014: Composite VORTEX2 supercell environments from near-storm soundings. *Monthly Weather Review*, **142 (2)**, 508–529, doi:10.1175/MWR-D-13-00167.1.

Poulos, G. S., and Coauthors, 2002: CASES-99: A comprehensive investigation of the stable nocturnal boundary layer. *B. Am. Meteorol. Soc.*, **83 (4)**, 555–581, doi:10.1175/1520-0477(2002)083⟨0555:CACIOT⟩2.3.CO;2.

Reif, D. W., and H. B. Bluestein, 2017: A 20-year climatology of nocturnal convection initiation over the central and southern great plains during the warm season. *Monthly Weather Review*, **145 (5)**, 1615–1639, doi:10.1175/MWR-D-16-0340.1.

Reuder, J., P. Brisset, M. Jonassen, M. Müller, and S. Mayer, 2009: The small unmanned meteorological observer SUMO: A new tool for atmospheric boundary layer research. *Meteorologische Zeitschrift*, **18 (2)**, 141–147.

Reuder, J., M. Jonassen, and H. Ólafsson, 2012: The small unmanned meteorological observer SUMO: Recent developments and applications of a micro-UAS for atmospheric boundary layer research. *Acta Geophys.*, **60 (5)**, 1454–1473, doi:10.2478/s11600-012-0042-8.

Richardson, S. J., F. V. Brock, S. R. Semmer, and C. Jirak, 1999: Minimizing errors associated with multiplate radiation shields. *J. Atmos. Ocean. Tech.*, **16 (11)**, 1862–1872, doi:10.1175/1520-0426(1999)016⟨1862:MEAWMR⟩2.0.CO;2.

Rodert, L. A., 1941: The effects of aerodynamic heating on ice formations on airplane propellers. Technical Report 799, National Advisory Committee for Aeronautics, Langley Aeronautical Lab. URL https://ntrs.nasa.gov/search.jsp?R=19930081671.

Saïd, F., U. Corsmeier, N. Kalthoff, C. Kottmeier, M. Lothon, A. Wieser, T. Hofherr, and P. Perros, 2005: ESCOMPTE experiment: intercomparison of four aircraft dynamical, thermodynamical, radiation and chemical measurements. *Atmos. Res.*, **74 (1)**, 217–252, doi:10.1016/j.atmosres.2004.06.012.

Scipión, D., 2011: Characterization of the convective boundary layer through a combination of large-eddy simulations and a radar simulator. Ph.D. thesis, The University of Oklahoma, 140 pp.

Shapiro, A., and E. Fedorovich, 2007: Katabatic flow along a differentially cooled sloping surface. *Journal of Fluid Mechanics*, **571**, 149–175.

Shapiro, M. A., 1984: Meteorological tower measurements of a surface cold front. *Mon. Weather Rev.*, **112 (8)**, 1634–1639, doi:10.1175/1520-0493(1984)112⟨1634:MTMOAS⟩2.0.CO;2.

Sinclair, V. A., S. Niemelä, and M. Leskinen, 2012: Structure of a narrow cold front in the boundary layer: Observations versus model simulation. *Monthly Weather Review*, **140 (8)**, 2497–2519, doi:10.1175/MWR-D-11-00328.1.

Steeneveld, G. J., R. J. Ronda, and A. A. M. Holtslag, 2015: The challenge of forecasting the onset and development of radiation fog using mesoscale atmospheric models. *Boundary-Layer Meteorology*, **154 (2)**, 265–289, doi:10.1007/s10546-014-9973-8, URL https://doi.org/10.1007/s10546-014-9973-8.

Straka, J. M., E. N. Rasmussen, and S. E. Fredrickson, 1996: A mobile mesonet for finescale meteorological observations. *Journal of Atmospheric and Oceanic Technology*, **13 (5)**, 921–936, doi:10.1175/1520-0426(1996)013⟨0921:AMMFFM⟩2.0.CO;2.

Stull, R., 1988: *An Introduction to Boundary Layer Meteorology*. 9th ed., Dordrecht.

Swean, T. F., and J. A. Schetz, 1979: Flow about a propeller-driven body in temperature-stratified fluid. *AIAA J.*, **17 (8)**, 863–869, doi:10.2514/3.61238.

Tanner, B. D., E. Swiatek, and C. Maughan, 1996: Field comparisons of naturally ventilated and aspirated radiation shields for weather station air temperature measurements. Conference on Agricultural and Forest Meteorology, Vol. 22, 227–230.

Thompson, D. W. J., and S. Solomon, 2005: Recent stratospheric climate trends as evidenced in radiosonde data: Global structure and tropospheric linkages. *Journal of Climate*, **18 (22)**, 4785–4795, doi:10.1175/JCLI3585.1.

Toms, B. A., J. M. Tomaszewski, D. D. Turner, and S. E. Koch, 2017: Analysis of a lower-tropospheric gravity wave train using direct and remote sensing measurement systems. *Monthly Weather Review*, **145 (7)**, 2791–2812, doi:10.1175/MWR-D-16-0216.1.

Trapp, R. J., D. J. Stensrud, M. C. Coniglio, R. S. Schumacher, M. E. Baldwin, S. Waugh, and D. T. Conlee, 2016: Mobile radiosonde deployments during the mesoscale predictability experiment (MPEX): Rapid and adaptive sampling of upscale convective feedbacks. *Bulletin of the American Meteorological Society*, **97 (3)**, 329–336, doi:10.1175/BAMS-D-14-00258.1.

van den Kroonenberg, A. C., S. Martin, F. Beyrich, and J. Bange, 2012: Spatially-averaged temperature structure parameter over a heterogeneous surface measured by an unmanned aerial vehicle. *Bound.-Lay. Meteorol.*, **142 (1)**, 55–77, doi:10.1007/s10546-011-9662-9.

Van der Veer Martens, B., B. G. Illston, and C. A. Fiebrich, 2017: The oklahoma mesonet: A pilot study of environmental sensor data citations. *Data Science Journal*, **16**, 47, doi:http://doi.org/10.5334/dsj-2017-047.

Vömel, H., and Coauthors, 2018: The NCAR / EOL community workshop on unmanned aircraft systems for atmospheric research. *UCAR/NCAR Earth Observing Laboratory*, doi:10.5065/D6X9292S.

Wainwright, C. E., T. A. Bonin, P. B. Chilson, J. A. Gibbs, E. Fedorovich, and R. D. Palmer, 2015: Methods for evaluating the temperature structure-function parameter using unmanned aerial systems and large-eddy simulation. *Boundary-Layer Meteorology*, **155 (2)**, 189–208.

Waugh, S., and S. Fredrickson, 2010: An improved aspirated temperature system for mobile meteorological observations, especially in severe weather. *25th Conf. on Severe Local Storms*, Denver, CO, Amer. Meteor. Soc., P5.2.

Wildmann, N., M. Hofsäß, F. Weimer, A. Joos, and J. Bange, 2014: MASC-a small remotely piloted aircraft (RPA) for wind energy research. *Adv. Sci. Res.*, **11**, 55, doi:10.5194/asr-11-55-2014.

Wildmann, N., G. A. Rau, and J. Bange, 2015: Observations of the early morning boundary-layer transition with small remotely-piloted aircraft. *Boundary-Layer Meteorology*, **157 (3)**, 345–373, doi:10.1007/s10546-015-0059-z, URL http://dx.doi.org/10.1007/s10546-015-0059-z.

Wood, N., 2000: Wind flow over complex terrain: A historical perspective and the prospect for large-eddy modelling. *Boundary-Layer Meteorology*, **96 (1)**, 11–32, doi:10.1023/A:1002017732694, URL https://doi.org/10.1023/A:1002017732694.

World Health Organization, 2016: Ambient air pollution: a global assessment of exposure and burden of disease.

Zhou, B., and F. K. Chow, 2012: Turbulence modeling for the stable atmospheric boundary layer and implications for wind energy. *Flow, Turbulence and Combustion*, **88 (1)**, 255–277, doi:10.1007/s10494-011-9359-7.

Zielke, B., 2011: A procedure for obtaining high-density in-situ measurements of ozone concentration within the planetary boundary layer. M.S. thesis, School of Meteorology, University of Oklahoma.